A STUDY OF FERMI SURFACES OF ReO_3 AND $Hg_{2.86}AsF_6$

By

FEREIDOON SAADATMAND RAZAVI, M.Sc.

A Thesis

Submitted to the Faculty of Graduate Studies

in Partial Fulfilment of the Requirements

for the Degree

Doctor of Philosophy

McMaster University

November 1978

A STUDY OF FERMI SURFACES OF ReO_3 AND $Hg_{2.86}AsF_6$

DOCTOR OF PHILOSOPHY (1978)
(Physics)

McMASTER UNIVERSITY
HAMILTON, ONTARIO

TITLE: A Study of Fermi Surfaces of ReO_3 and $Hg_{2.86}AsF_6$

AUTHOR: Fereidoon Saadatmand-Razavi, B.Sc., (University of Meshed, Iran), M.Sc., (McMaster University)

SUPERVISOR: Professor W. R. Datars

NUMBER OF PAGES: xii, 111

ABSTRACT

The Fermi surfaces of ReO_3 and $Hg_{2.86}AsF_6$ have been studied. Open orbits have been observed in ReO_3 in magnetic fields up to 5.5 T by the induced torque method. The experimental results show that the third band Fermi surface of ReO_3 is connected along the <100> directions as predicted by Mattheiss' augmented-plane-wave band structure calculation. de Haas-van Alphen frequencies of ReO_3 have been measured as a function of pressure up to 5 kbar with the magnetic field along the [111] and [001] crystallographic directions. The variation of the frequencies with pressure is linear at low pressure and for the α frequencies follows free electron scaling predictions. Above 3 kbar, all cross sectional areas increase much faster with pressure. The area compressibilities are one order of magnitude higher than the low pressure area compressibilities. The Dingle temperature and the g-factor along [111] in ReO_3 were measured as a function of pressure up to 5 kbar. The resistivity of ReO_3 was also measured as a function of pressure at room tmperature and at 110 K. The increase in the de Haas-van Alphen frequencies of ReO_3 above 3 kbar may be attributed to an increase in covalent bonding or a rotation of the oxygen atoms at high pressure. Measurement of the de Haas-van Alphen effect, at 1.1 K, in the linear-chain mercury compound $Hg_{2.86}AsF_6$ indicates that the Fermi surface

consists of a set of cylinders with axes along the c-axis. The multiplicity of cylinders is shown to arise from a translation of the Fermi surface sheets by a superlattice formed by the incommensurate mercury chains.

ACKNOWLEDGEMENTS

I wish to express my gratitude to my supervisor, Dr. W. R. Datars not only for his guidance but also for his keen interest throughout my research and also for his actual help in the revisions and corrections to this thesis. A sincere thank-you is especially due to Dr. Zaven Altounian for his genuine assistance. I also want to thank Dr. A. G. Berlinski, U.B.C., for discussing his results on the $Hg_{2.86}AsF_6$ compound prior to publication.

Many discussions among the members of the Fermi surface group have been stimulating and fruitful - my thanks to all my fellow students. Mr. C. Verge proved to be a source of bottomless knowledge and his unreserved willingness to help with any technical problems is deeply appreciated. I thank Eléonore sincerely for her help and encouragement throughout this work.

This research was supported by a research grant from the National Research Council of Canada.

TABLE OF CONTENTS

LIST OF TABLES

LIST OF FIGURES

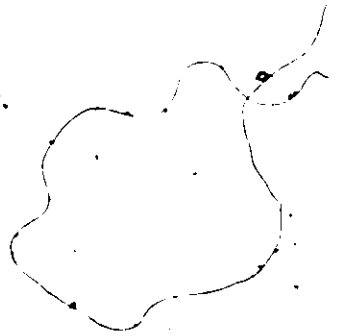

SECTION 1

STUDY OF FERMI SURFACE OF ReO_3

CHAPTER I

INTRODUCTION

The compound ReO_3 is a red transition metal oxide, which exhibits metallic electrical conductivity. In addition to its importance as a transition metal oxide, ReO_3 is interesting because of its relatively simple cubic crystal structure. This structure is closely related to certain classes of materials such as the perovskites (ABO_3) and the tungsten bronzes (A_xWO_3) where A is an alkali metal, copper or silver.

Single crystals of ReO_3 were first prepared by Ferretti et al.(1965). They found that the electrical conductivity at 77°K was 2.5×10^6 $(\Omega\ cm)^{-1}$. This is the same order of magnitude as the conductivity of copper. Further work was done in ReO_3 using nuclear magnetic resonance by Narath and Barham (1968) who found that the conduction electron states of ReO_3 at the Fermi level are derived mainly from atomic d states. They also found that the conduction band of the metals ReO_3 and Na_xWO_3 are very similar. Mattheiss (1969) carried out a band structure calculation for ReO_3 based on the augmented plane wave (APW) method.

The APW band calculation showed that strong molecular bonding, due to the overlap of the rhenium 5d and oxygen 2p

atomic orbitals, contributes to the broadening of the 5d conduction band leading to the metallic conductivity. The band calculation also showed that the Fermi surface consists of three electron-like Fermi surface sheets α, β and γ. The α and β Fermi surface sheets are roughly spherical and are centred at Γ in the first and second zones. The γ Fermi surface in the third zone consists of <100> directed cylinders intersecting at Γ and forms a multiply-connected electron surface in the extended zone scheme.

This model of the Fermi surface of ReO_3 has been supported by the de Haas-van Alphen (dHvA) measurements of Marcus (1968) and Philips and Shanks (1971) as well as by magnetothermal oscillation measurements of Graebner and Greiner (1969). The existence of open orbits is the most direct evidence of the multiply-connected electron sheet. The induced torque method (Moss and Datars 1967) has proven to be a most powerful technique for the observation of open orbits because at high fields the torque increases proportional to B^2 in the presence of open orbits and saturates when the orbits are closed. The open orbit studies are also of interest because the γ-Fermi surface sheet of ReO_3 is similar to the three-dimension grid considered by Lifshitz and Peschanskii (1958) in describing the effects of the topology of the Fermi surface on the galvanomagnetic properties of metals.

The pressure dependence of dHvA spectrum of a given metal can serve as a valuable tool in determining the validity of energy band calculations (Harrison, 1965) as well as for observation of structural phase transitions (Slavin and Datars, 1974) and electronic phase transitions (Lifshitz, 1960, Schirber and Switendick, 1970). The dHvA frequency is directly proportional to the cross-sectional area of the Fermi surface, thus, the pressure derivative of the Fermi surface cross section (area compressibility) can be obtained from the pressure dependence of the dHvA frequency.

The hydrostatic pressure derivatives of the Fermi surface cross section for ReO_3 were measured up to 25 bar by the fluid helium phase-shift method (Schirber et al., 1972). This work extends the effect of pressure on the Fermi surface of ReO_3 to 5 kbar.

The Landé spin splitting or the effective g-factor, the Dingle temperature and the resistivity as a function of pressure up to 5 kbar were also measured in order to obtain additional information about an anomalous increase of Fermi surface of ReO_3 at high pressure observed during this work.

Chapter II provides a brief theoretical background of magnetoresistance, the dHvA effect, the effect of high pressure on the Fermi surface of metals and the Fermi surface of ReO_3. In Chapter III the experimental methods are discussed. These

include the experimental technique for crystal growth, the torque magnetometer and dHvA system. Chapter IV gives experimental results and discussions of open orbits and induced torque in ReO_3. The experimental results of the pressure dependence of the Fermi surface of ReO_3 are presented and discussed in Chapter V. Chapter VI contains the conclusions of the study.

CHAPTER II

THEORY

a. Magnetoresistance in High Field Region

In the presence of a magnetic field, the conduction electron experiences a Lorentz force

$$\vec{F} = \frac{d\hbar\vec{k}}{dt} = e\ \vec{v}\times\vec{B} \qquad \text{(II-1)}$$

where $\vec{k}$ is the wave vector of the electron and $\hbar\vec{k}$ is the crystal momentum. The group velocity, $\vec{v}$, of the electron is related to the surface of constant energy $\varepsilon(\vec{k})$ (Fermi surface) by the relation

$$\vec{v} = \frac{d\vec{r}}{dt} = \frac{1}{\hbar}\nabla_{\vec{k}}\varepsilon(\vec{k}) \ . \qquad \text{(II-2)}$$

The above expressions show that the representative point k moves in an orbit confined by the intersection of the Fermi surface with a plane normal to $\vec{B}$. If the electron is not scattered, it moves in a closed orbit with the period

$$T = \frac{2\pi}{\omega_c} = \frac{\hbar}{eB}\oint_{\text{orbit}} \frac{d\vec{t}}{v_\perp} \qquad \text{(II-3)}$$

where ω_c is the cyclotron frequency and $v_\perp$ is the component of $\vec{v}$ perpendicular to $\vec{B}$ and to the Fermi surface tangent at the

point k. For a free electron:

$$\omega_c = \frac{eB}{m} \qquad \text{(II-4)}$$

where m is the mass of the free electron. In the crystal environment, the cyclotron frequency is defined by

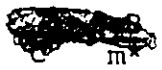

$$\text{(II-5)}$$

where m* is the effective mass of the electron and is given by

$$m^* = \frac{1}{2\pi} \frac{\partial A}{\partial \varepsilon} \; . \qquad \text{(II-6)}$$

In the above expression, A is the cross sectional area of the Fermi surface in momentum space. By integrating equation II-1 using II-2, the relation between the orbit in momentum space and real space can be expressed by

$$\vec{r} \times \frac{e\vec{B}}{\hbar} = -(\vec{k}-\vec{k}_o) \; . \qquad \text{(II-7)}$$

Therefore, the projection of the real space orbit on a plane perpendicular to $\vec{B}$ is similar to that in momentum space except for a factor $\frac{eB}{\hbar}$ and a rotation by $\frac{\pi}{2}$. Different types of orbits exist; for example, consider the Fermi surface constructed by the intersecting tubes, Fig. 1. When the magnetic field is normal to the plane of the paper (along the z-direction), the Fermi surface supports two kinds of orbits, an electron-like and a hole-like orbit (Fig. 1a). For other directions of

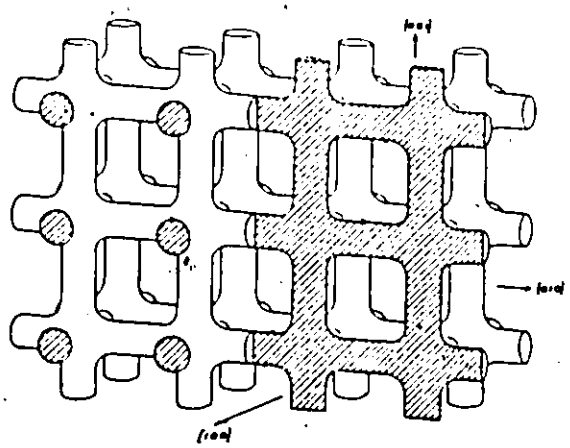

Fig. a

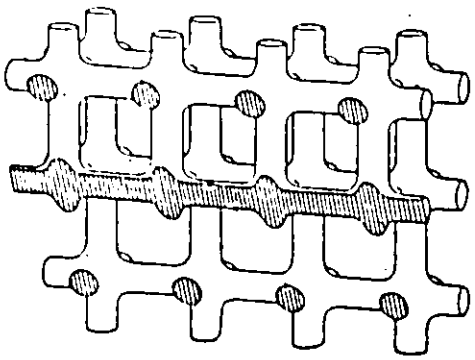

Fig. b

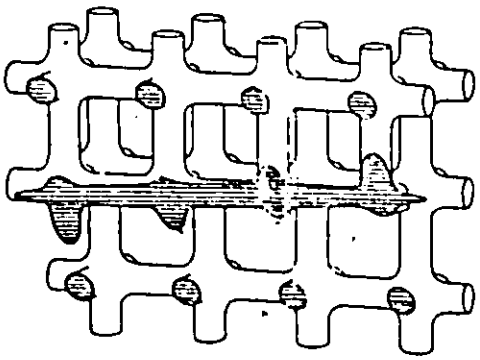

Fig. c

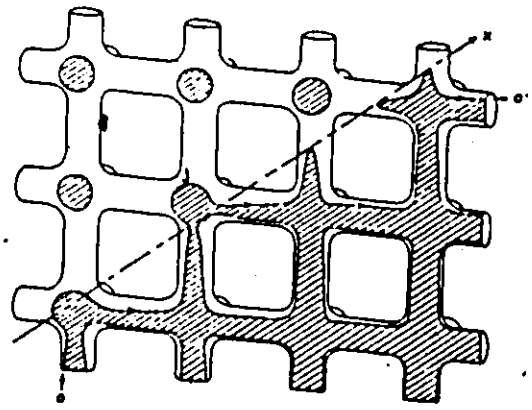

Fig d

Figure 1

Possible type of open orbits for a cubic metal.

the field, there are open orbits which go out to infinite distance in momentum space, and extended orbits which are closed but extend through several Brillouin zones (Figs. 1b, c and d). In order for the electron to explore an orbit before being scattered by phonons, impurities and lattice imperfection, the sample must be in the high field region. The high field region is defined by

$$\omega_c \bar{\tau} >> 1 \qquad \text{(II-8)}$$

where $\bar{\tau}$ is the average relaxation time around each orbit. In an applied electromagnetic field, the current is related to the electric field by the conductivity tensor

$$J_i = \sigma_{ij} E_j \ . \qquad \text{(II-9)}$$

In the high field region, σ_{ij} can be expanded in a power series of the dimensionless parameter γ (Lifshitz et al., 1956).

$$\sigma_{ij} = a^0_{ij} + a^1_{ij}\gamma + a^2_{ij}\gamma^2 \qquad \text{(II-10)}$$

where γ is given by

$$\gamma = \frac{1}{\omega_0 \bar{\tau}} = \frac{m_o}{e\bar{\tau}} \cdot \frac{1}{B} \ . \qquad \text{(II-11)}$$

Fawcett (1964) obtained the conductivity and resistivity tensors in the high field region by retaining only the leading terms of each component of the conductivity and resistivity tensors. For compensated metals, the resistivity tensor in the high field region is

$$\underset{\substack{\gamma \to 0 \\ B \to \infty}}{\text{Lt}}\ \rho_{ij} = \begin{vmatrix} \nu_\gamma^{-2} & \nu_\gamma^{-2} & \nu_\gamma^{-1} \\ \nu_\gamma^{-2} & \nu_\gamma^{-2} & \nu_\gamma^{-1} \\ \nu_\gamma^{-1} & \nu_\gamma^{-1} & \nu_\gamma^{0} \end{vmatrix} = \begin{vmatrix} \nu_B^{2} & \nu_B^{2} & \nu_B \\ \nu_B^{2} & \nu_B^{2} & \nu_B \\ \nu_B & \nu_B & \nu_B^{0} \end{vmatrix} \qquad \text{(II-12)}$$

and for uncompensated metals it is

$$\underset{\substack{\gamma \to 0 \\ B \to \infty}}{\text{Lt}}\ \rho_{ij} = \begin{vmatrix} B^0 & -\frac{B\Omega}{en_A} & \nu_B^0 \\ \frac{B\Omega}{en_A} & \nu_B^0 & \nu_B^0 \\ \nu_B^0 & \nu_B^0 & \nu_B^0 \end{vmatrix} \qquad \text{(II-13)}$$

where n_A is the number of charge carriers and Ω is the volume of a unit cell of the Bravais lattice.

In the presence of open orbits (along the x direction) the resistivity tensor for both compensated and uncompensated metals is given by

$$\underset{\substack{\gamma \to 0 \\ B \to \infty}}{\text{Lt}}\ \rho_{ij} = \begin{vmatrix} \nu_\gamma^{-2} & \nu_\gamma^{-1} & \nu_\gamma^{-1} \\ \nu_\gamma^{-1} & \nu_\gamma^{0} & \nu_\gamma^{0} \\ \nu_\gamma^{-1} & \nu_\gamma^{0} & \nu_\gamma^{0} \end{vmatrix} = \begin{vmatrix} \nu_B^{2} & \nu_B & \nu_B \\ \nu_B & \nu_B^{0} & \nu_B^{0} \\ \nu_B & \nu_B^{0} & \nu_B^{0} \end{vmatrix} \qquad \text{(II-14)}$$

Thus in the high field region ρ_{xx} goes to infinity, while ρ_{yy} and ρ_{zz} saturate.

The asymptotic dependence of the resistivity tensor on the magnetic field is tabulated in Table I.

Table I. The field dependence of the galvanomagnetic properties of metals in the high field limit

	All closed orbits		Open Orbits[a]
	Uncompensated $n_e \neq n_n$	Compensated $n_e = n_n$	
ρ_{xx}	B^0	B^2	$a, B^2\cos^2\alpha + a_2$
ρ_{yy}	B^0	B^2	$b, B^2\sin^2\alpha + b_2$
ρ_{zz}	B^0	B^0	B^0
ρ_{xy}	B	B^2	B

[a] In k space the direction of open orbits makes an angle α with the x axis.

b. de Haas van Alphen Effect (dHvA)

In 1932, de Haas and van Alphen discovered the oscillatory behaviour of the magnetic susceptibility of a bismuth single crystal at liquid hydrogen temperature. Later experiments on different metals showed that this effect (dHvA) is not only the property of single crystal bismuth in a magnetic field, but, at very low temperatures, the magnetic properties of all high-purity single crystal metals oscillate as the magnetic field H is varied.

The motion of an electron in the presence of the magnetic field (along the z direction) was discussed in the previous section. Equation (II-7) gives the relation between the orbit of an electron in k-space and real space. The Bohr-Sommerfeld quantization rule gives

$$\oint pdq = \oint (\hbar\vec{k} - e\vec{A}) \cdot d\vec{r} = (n+\gamma) 2\pi\hbar \qquad \text{(II-15)}$$

where H = curl A and γ is a phase factor ($\gamma = \frac{1}{2}$ for free electron). Substituting (II-7) in (II-15) and integrating the above quantum condition becomes

$$\phi = (n+\gamma) 2\pi\hbar/e \qquad \text{(II-16)}$$

where ϕ is the magnetic flux passing through the projected orbit in real space. On evaluating the flux in terms of the area A in k space (using (II-7)), one can obtain the Onsager quantum condition (Onsager 1952).

$$A_n = \frac{2\pi eH}{\hbar} (n+\gamma). \qquad \text{(II-17)}$$

The above result is independent of k_z. Therefore, the allowed states fall on tubes with cross sectional areas given by (II-17). The energy for a given k can be written into two terms: the orbital part of the energy which is quantized into the Landau levels and $\varepsilon(k_z)$. (For a free electron $\varepsilon(k_z) = \frac{\hbar^2 k_z^2}{2m}$)

$$\varepsilon_n = (n+\gamma)\hbar\omega_c + \varepsilon(k_z). \qquad \text{(II-18)}$$

The Landau levels are highly degenerate and the degeneracy changes with magnetic field strength. As the magnetic field H increases, the energy of the Landau levels increases, eventually, the energy of the outermost Landau level reaches the Fermi energy and empties when it passes the Fermi level. This causes the free energy of the electron to oscillate about its zero field energy as the magnetic field changes. The frequency of the oscillation is given by

$$F = \frac{\hbar}{2\pi e} A_o \qquad \text{(II-19)}$$

where A_o is the extremal cross sectional area of the Fermi surface normal to the magnetic field. In a magnetic field H and with a temperature T, the complete expression for the oscillatory behaviour of the free energy is given by the Lifshitz and Kosevich (LK) formula (Lifshitz and Kosevich (1955)

$$\tilde{\Omega}_{osc} = -\left(\frac{H^2}{2\pi F}\right) D(H) \sum_{r=1}^{\infty} \frac{I_r k_r}{r^{5/2}} \cos\left[2\pi r\left(\frac{F}{H} - \gamma\right) \mp \frac{\pi}{4}\right] \cos\left(\frac{r\pi g}{2} \frac{m^*}{m}\right)$$

where

$$D(H) = -\frac{e\hbar A}{4\pi^4 m^*} \left(\frac{2\pi eH}{\hbar}\right)^{1/2} \left|\frac{\partial^2 A}{\partial k_z^2}\right|^{-1/2} \qquad \text{(II-20)}$$

In this expression, r is the harmonic number, the - and + signs in the sin terms are used for the maximum and minimum cross sectional area, respectively, and $\left|\frac{\partial^2 A}{\partial k_z^2}\right|$ is the curvature factor of the Fermi surface at the extremum.

I_r represents the temperature dependence of the dHvA effect and is given by

$$I_r = \frac{X_r}{\sinh X_r} \qquad \text{(II-21)}$$

where $X_r = 2\pi^2 r \frac{k_B T}{e\hbar} \frac{m^*}{H} = 14.69 \frac{rm^*T}{H}$. ($k_B$ is the Boltzmann factor).

The broadening of the Landau level by various types of electron scattering in the crystal is described by

$$k_r = \exp\left(-2\pi^2 r \frac{k_B T_D m^*}{e\hbar H}\right)$$

$$= \exp(-14.69\ r\ m^* T_D/H) \qquad \text{(II-22)}$$

where the Dingle temperature T_D is related to the half width (Γ) of the Lorentzian curve describing the broadening of the Landau levels and is

$$T_D = \frac{\Gamma}{\pi k_B} \qquad \text{(II-23)}$$

Finally, the factor $\cos\left(\frac{r\pi}{2} g \frac{m^*}{m}\right)$ is the correction factor for the Zeeman splitting of the Landau levels due to the electron

spin interaction with the magnetic field. g is the splitting factor and for free electrons is equal to 2.0023. The expression for the magnetization can be derived by calculating the gradient of the free energy with respect to H. The magnetization (in polar coordinates) is

$$\tilde{M} = D(H)\left[\hat{H} - \frac{1}{F}\frac{\partial F}{\partial \theta}\hat{\theta} - \frac{1}{F\sin\theta}\frac{\partial F}{\partial \phi}\hat{\phi}\right]$$

$$\times \sum_{r=1}^{\infty} \frac{I_r k_r}{r^{3/2}} \sin\left[2\pi r\left(\frac{F}{H} - \gamma\right) \mp \frac{\pi}{4}\right] \qquad \text{(II-24)}$$

In the above calculation only the cosine terms were considered since the amplitude of the cosine term does not change as rapidly as the cosine term with the magnetic field.

c. The Effect of the Hydrostatic Pressure on the Fermi Surface of Metals

The effect of hydrostatic pressure causes a change of the lattice constant of a crystal. Since the energy bands of electrons in a crystal are determined by the properties of the ions and the distance between them in the crystal lattice, the change in the lattice constant (position of the ions) results in a change in the energy bands of the solid.

In the free electron model, the Fermi surface is defined by a sphere of radius k_F

$$V_F = \frac{4}{3}\pi K_F^3 . \qquad \text{(II-25)}$$

A crystal consists of N primitive cells and volume V. The

volume of the first Brillouin zone is $(\frac{8\pi^3}{V})$ and contains N allowed wave vectors. Considering the spin of the electron, the total number of electrons that can be accommodated in the Fermi sphere is

$$2 \times \frac{4}{3} \pi k_F^3 / (8\pi^3/V) = \frac{V}{3\pi^2} k_F^3 = N$$

or

$$k_F = (\frac{3\pi^2 N}{V})^{1/3} \qquad \text{(II-26)}$$

Using the Harrison construction (Harrison 1966), segments of the Fermi surface in different zones can be obtained.

Equation (II-26) shows that the radius of the Fermi sphere is inversely proportional to the cube root of the volume of the unit cell. Under hydrostatic pressure, i.e. isotropic compression, the Fermi sphere grows as the volume is compressed. The Brillouin zone also becomes larger since the lattice wave numbers are inversely proportional to the lattice constant. Thus the shape of the Fermi surface sheets remain the same for a cubic metal and the effect of hydrostatic pressure is simply to scale the size of the Fermi surface sheets.

The dHvA experiments under hydrostatic pressure give us some information about the cross sectional area of the Fermi surface with pressure. In the free electron model for the cubic system, the scaling factor α is given by

$$\alpha = \frac{a(P)}{a_0} \tag{II-27}$$

where a_0 is the value of the lattice constant at zero pressure. The zero pressure area compressibility is defined by

$$\frac{1}{A_{F_0}} \frac{dA_F}{dp} = \frac{-2}{\alpha} \frac{d\alpha}{dp} \tag{II-28}$$

and the expression for the volume compressibility is

$$k_T = -\frac{1}{V}\frac{dV}{dp} = -\frac{3}{\alpha}\frac{d\alpha}{dp} = -\frac{3}{2}\frac{1}{A_F}\frac{dA_F}{dp}$$

$$\therefore \quad \frac{1}{A_{F_0}}\frac{dA_F}{dp} = +\frac{2}{3}k_T$$

or

$$\frac{1}{F_0}\frac{dF}{dp} = +\frac{2}{3}k_T \tag{II-29}$$

since the cross section of the Fermi surface normal to the magnetic field is proportional to the dHvA frequency. Using the free electron model (non transition metal), one can obtain some information about the sign as well as an estimation of the magnitude of the pressure effect. The above result is only true for the free electron model; in general, the cross sectional area of the Fermi surface can be written in terms of the Fermi energy ε_F, the lattice potential U_i and the spin orbit parameter λ (Anderson et al, 1967). Since the area is usually calculated in units of $(\frac{2\pi}{a})^2$ one can write

$$A = \left(\frac{2\pi}{a}\right)^2 A_0(E_F, V_i, \lambda) \quad . \tag{II-30}$$

Thus, the relative change of the area with pressure is

$$\frac{1}{A}\frac{dA}{dp} = -\frac{2}{3}k_T + \frac{1}{A_0}\left(\frac{\partial A_0}{\partial \epsilon_F}\frac{\partial \epsilon_F}{\partial p} + \sum_i \frac{\partial A_0}{\partial V_i}\frac{\partial V_i}{\partial p} + \frac{\partial A_0}{\partial \lambda}\frac{\partial \lambda}{\partial p}\right) \quad . \tag{II-31}$$

This result indicates that the experimental value of the area compressibility may deviate from the $\frac{2}{3}$ law. The shape of the Fermi surface is an important factor in determining the effect of pressure. For a spherical Fermi surface sheet, the zero pressure area compressibility follows the $\frac{2}{3}$ law. However, for a complicated Fermi surface, the $\frac{2}{3}$ law is no longer valid and one should use eq. (II-31). Valuable information about the energy band parameters can be obtained by fitting the theoretical result to eq. (II-31). Especially, this fitting procedure gives a direct test of the accuracy of the method of constructing the crystal potential.

d. The Energy Bands and Fermi Surface of ReO_3

Rhenium trioxide (ReO_3) is a member of the perovskite compounds with the chemical formula ABC_3. These compounds crystallize in the simple cubic system where the B atom is at the origin, C atoms are at each of the face centers and the A atoms are at the corners of the simple cubic unit cell.

The ReO_3 structure is formed by removing the A atoms from the array of ABC_3. This compound is metallic with a high conductivity at room temperature. Properties of ReO_3 are given in Table II.

Table 2. Properties of ReO_3

Property	Value
Colour	Red
Density	6.91 gms/cc
Resistivity at 296 K	7.8×10^{-6} ohm cm
Bravais Lattice	Simple cubic
Unit Cell Dimension at 296 K	3.743 Å

Following the successful attempt by Ferretti et al (1965) to crystallize the ReO_3 compound, the NMR results of Narath and Barham (1968) showed that the conduction bands are derived mainly from the atomic d states. The dHvA experiment (Marcus 1968) and the magnetothermal oscillations (Graebner et al,1969) in ReO_3 as well as the optical measurement of Feinleib et al (1968) provided useful information about the Fermi surface and energy band structure of this compound.

The band calculation was carried out by Mattheiss (1969). He used the augmented plane wave (APW) method to obtain the energy at symmetry points in the Brillouin zone. In the APW calculation, the crystal potential V(r) separated into a spherically symmetric part inside the APW sphere centered about each atomic site plus a correction $V_\Delta(r)$ outside the APW spheres. Mattheiss obtained the energy bands throughout the Brillouin zone by fitting the APW results at the symmetry points to the energy bands obtained from the Slater-Koster LCAO (linear combination of atomic orbitals) calculations. In the LCAO tight binding interpolation scheme 14 basis functions were involved which included 5 rhenium 5d orbitals and nine oxygen 2p orbitals. Twenty parameters were involved in the LCAO energy band calculation. These parameters represent the first nearest neighbour rhenium-rhenium d-d interactions, nearest neighbour and second nearest neighbour oxygen-oxygen (p-p) interactions nearest neighbour oxygen-rhenium (p-d) interactions and the effect

of spin-orbit coupling among the rhenium 5d states.

At his final stage of calculation, Mattheiss (1969) used optical data (Feinleib et al,1968) and cyclotron mass data (Marcus 1968) in order to adjust the L@AO parameters which involve the separation between the oxygen 2p and rhenium 5d energy band states as well as the corresponding band width.

The energy band calculation showed that the Fermi surface consists of 3 electron-like Fermi surface sheets, α, β and γ Fig. 2. The α and β are roughly spherical and are centered at Γ in the first and second zones. The γ Fermi surface sheet in the third zone consists of <100> directed cylinders intersecting at Γ and form a multiply-connected electron surface in the extended zone scheme. The γ sheet has two closed extremal orbits when the magnetic field is along the [100] direction. One is electron-like γ_1, and the other is hole-like γ_2. Another extremal orbit γ_3 which is electron-like exists on the γ sheet when the magnetic field is near the [111] direction.

In addition to these orbits, Mattheiss (1969) predicted an orbit which involves magnetic breakdown from the β to the γ Fermi surface sheets when the magnetic field is along the [110] direction.

The dHvA results of Marcus (1968), and Philips and Shanks (1971) are within 5% of the theoretical calculations of Mattheiss. The breakdown orbit was observed in a dHvA experiment by Razavi and Datars (1976). The angular dependence of

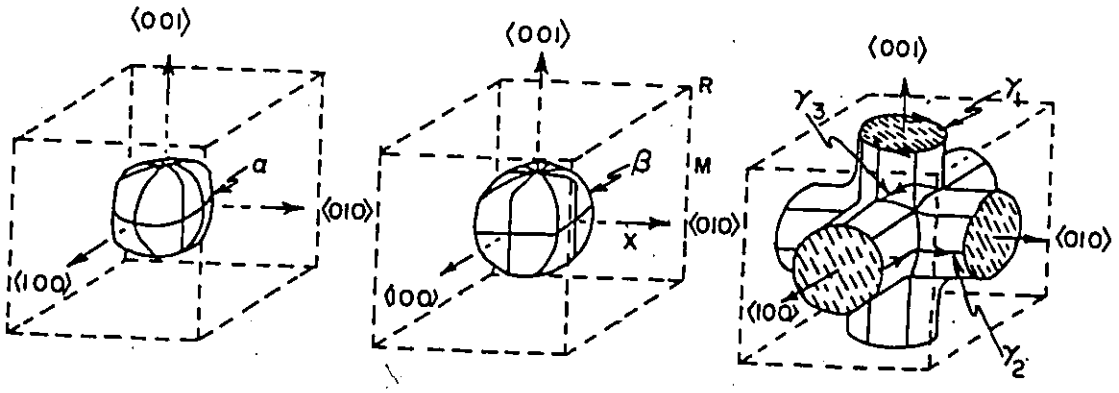

Figure 2

Three dimensional sketches of the three electron sheets of the APW Fermi surface in ReO_3.

the dHvA frequencies in the (110) plane is shown in fig. 3. The γ_1-β frequency in figure 3 corresponds to the magnetic breakdown between γ and β orbits.

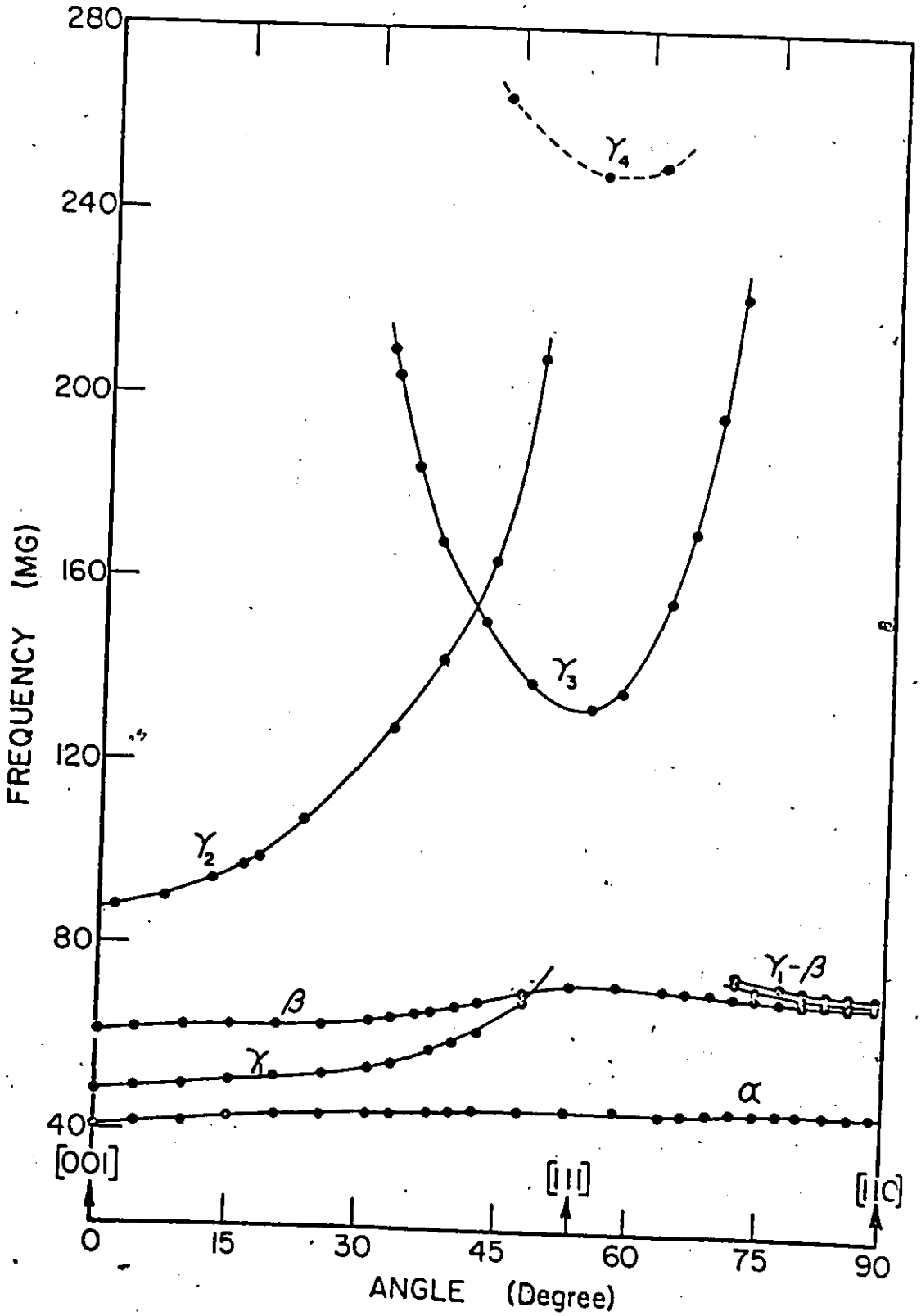

Figure 3

dHvA frequencies of ReO_3 in the (110 plane).

CHAPTER III

EXPERIMENTAL METHOD

a. Single Crystal Growth

The ReO_3 crystals were grown by the iodine vapour transport technique following the procedure used by Ferretti (1965). Single crystals of a compound are obtained by disturbing the equilibrium condition (e.g. by using a temperature gradient) between the solid phase and gaseous components. The ReO_3 compound reacts with iodine at 380°C; the reaction is reversible at 370°C. The probable reaction is (Quinn and Neiswander,1970)

$$ReO_{3(s)} + 2I_{2(g)} \underset{370°C}{\overset{380°C}{\rightleftharpoons}} ReOI_{4(g)} + O_{2(g)} \qquad \text{(III-1)}$$

ReO_3 charge material with a purity of 99.997% and iodine of analytic reagent quality were used for growing ReO_3 single crystals. The samples were grown in a quartz tube of 1 cm diameter and 20 cm length. The ratio of 10 to 1 of the ReO_3 powder to the iodine was chosen in order to increase the growth rate of ReO_3 crystal (Ferretti et al,1965, Quinn et al,1970). The quartz ampule was evacuated to 10^{-5} torr and sealed off before placing it in a furnace. The furnace had three independently controlled zones. Initially the temperature of

the growth zone (380°C) was set higher than the charge zone (360°C) in order to keep the number of ReO_3 nuclei to a minimum prior to crystal growth. The procedure was reversed after 24 hours and the temperature of the charge and growth zones were set at 380±1 and 370±1, respectively. Transport of ReO_3 was allowed to continue for 20 days after which the furnace was shut off and the ampule allowed to cool to room temperature. Several single crystals of ReO_3 of different sizes were obtained. Some were cubic in shape of a side dimension of about 1 mm and a plane had a side dimension of 2 mm. They were washed with absolute ethyl alcohol to remove any excess of iodine.

b. Induced Torque Technique

It is well established that the torque technique can provide some information about the galvanomagnetic properties and the topology of the Fermi surface of metals (Moss and Datars, 1967). An induced eddy current in the sample is created by the rotation of the magnet about the y axis (in xz plane) with the sample suspended along this axis or by rotating the sample about the y axis in a static magnetic field directed along the z axis. The induced eddy current in the sample produces a retarding torque which is measured by the torque magnetometer.

Vischer and Falicov (1970) calculated the induced torque for a homogeneous spherical sample of radius R. They showed that for the magnetic field along the z axis the induced torque is

$$N_y = (2\pi \frac{R^5}{15}) B^2 \Omega \bar{\sigma}_{xx} \qquad \text{(III-2)}$$

where B is the magnetic field and Ω is the frequency of the rotation. The effective conductivity tensor $\bar{\sigma}_{xx}$ is defined by

$$\bar{\sigma}_{xx} = \frac{1}{2} \left[(T_r \overleftrightarrow{\rho}) I - \overleftrightarrow{\rho}^{\dagger} \right]^{-1}_{xx} \qquad \text{(III-3)}$$

where $\overleftrightarrow{\rho}$ is the resistivity tensor and $\rho^{\dagger}$ is the transpose of the tensor $\overleftrightarrow{\rho}$. By substituting the components of the resistivity tensor $\overleftrightarrow{\rho}$ and considering no transverse mixing ($\rho_{xz} = \rho_{yz} = \rho_{zy} = \rho_{zx} = 0$) $\bar{\sigma}_{xx}$ can be written as

$$\bar{\sigma}_{xx} = \frac{2(\rho_{xx}+\rho_{zz})}{(\rho_{xx}+\rho_{zz})(\rho_{yy}+\rho_{zz})+\rho_{xy}\rho_{yx}} . \qquad \text{(III-4)}$$

In the high field limit, eq.(II -14) shows that $\rho_{xx} >> \rho_{zz}$ with an open orbit along the K_x axis and equation (III-4) reduces to

$$\bar{\sigma}_{xx} = \frac{2\rho_{xx}}{\rho_{xx}(\rho_{yy}+\rho_{zz})+\rho_{xy}^2} . \qquad \text{(III-5)}$$

If the direction of the open orbit makes an angle α with the x axis, the asymptotic behaviour of the induced torque and $\bar{\sigma}_{xx}$ for compensated and uncompensated material are

$$N = d_1 B^2 \cos^2\alpha + d_2$$

$$\bar{\sigma}_{xx} = C_1 \cos^2\alpha + C_2 B^{-2} \qquad \text{(III-6)}$$

where C_1, C_2, d_1 and d_2 are constants. Therefore, the induced torque increases proportionally to B^2 in the presence of open orbits and saturates in their absence. This property of the induced torque in the high field limits makes it possible to distinguish the presence of open orbits in metals directly.

The induced torque was measured with the magnetometer constructed by C. Verge for use in a superconducting magnet. The sample was mounted inside a rotating coil which is able to rotate over a range of ± 100° about the y axis, Fig. 4. In order to detect directly the induced torque and to eliminate background torque as well as de Haas-van Alphen torque, a positional angle modulation is used. In this technique the sample moves back and forth at a modulation frequency ω while the sample is rotating. Then, the induced torque signal is detected at the frequency ω by a phase sensitive detector and recorded directly on a chart recorder. The details of electronic processing has been described by Verge et al (1977). Another feature of this torque magnetometer is the capability of changing the orientation of the sample, while it is inside the coil. This is done with a screwdriver-type mechanism that can be put in contact with the sample holder. The ReO_3 crystal used in the torque experiment, had the dimensions of $1.8 \times 1.6 \times .8$ mm^3. The sample was oriented by x-rays using the Laue back reflection technique and was mounted inside the sample holder by General Electric cement. The experiment was

Figure 4

Diagram of torque magnetometer's rotating coil. (a) 0° rest position; (b) 90° from rest position. M_1 and M_2 are two orthogonal modulation coils. L are the electrical connections to the modulation coils.

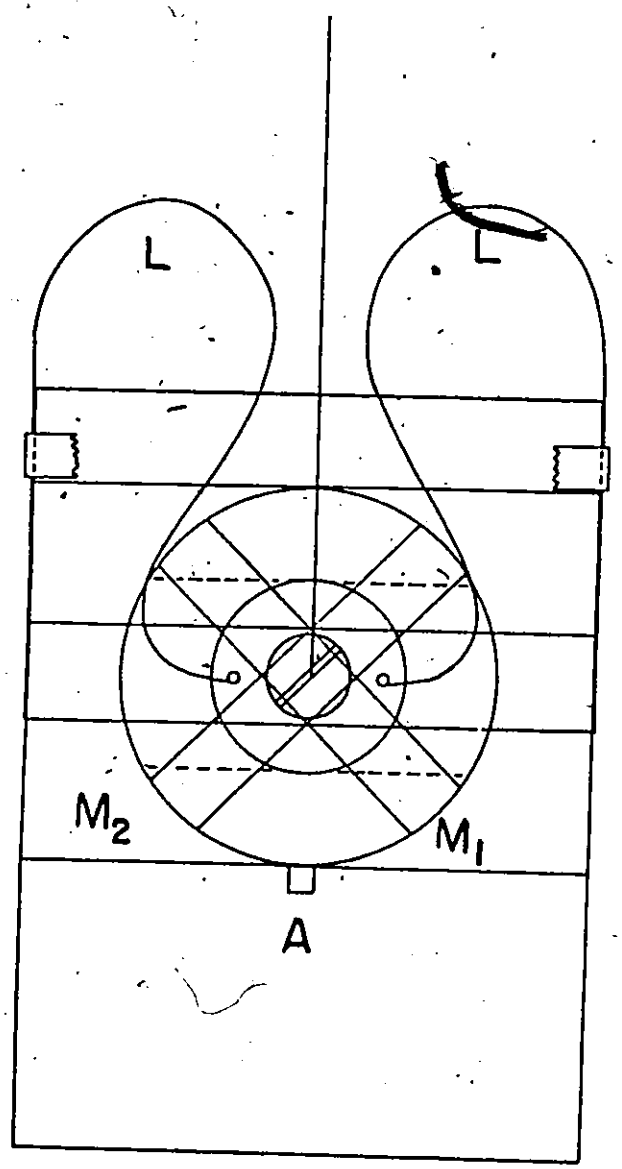

(a)

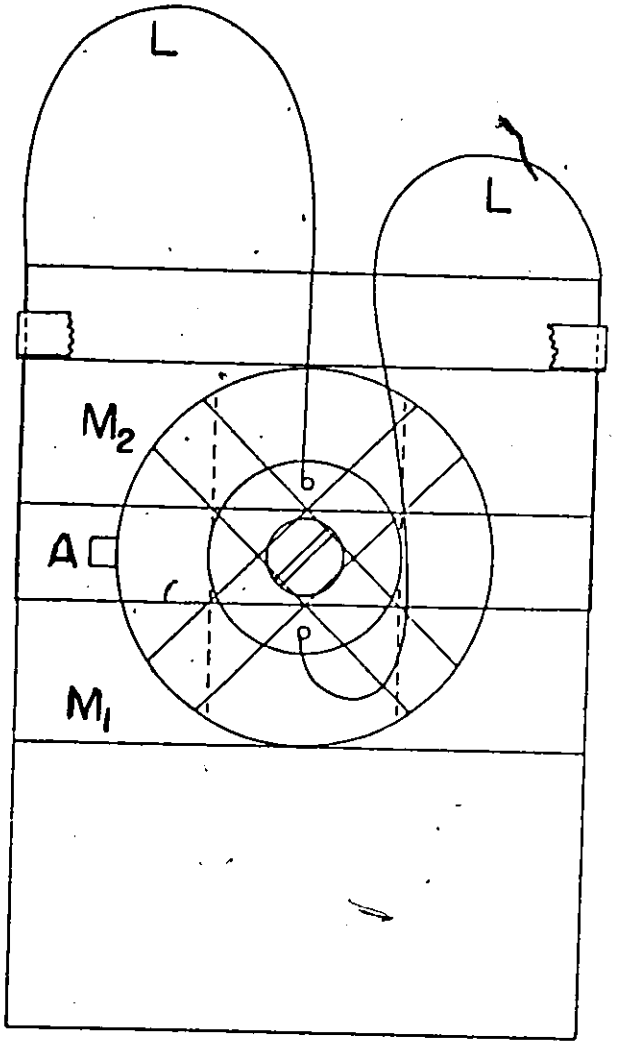

(b)

carried out in a 5.5 T Westinghouse superconducting magnet. The sample was rotated at a rate of 25°/min. The induced torque signal was detected at a modulation frequency of 10 Hz with an amplitude of 2.5° peak to peak. Different crystallographic planes were studied by rotating the crystal about the [110] direction.

c. dHvA Detection Technique

The dHvA technique was used to study the effect of pressure on the Fermi surface of ReO_3. In order to observe the dHvA effect experimentally, one must measure the quantum magnetization of the sample as a function of applied D.C. magnetic field H. This can be done by measuring the time derivative of the magnetization M by superimposing a modulation field $h\cos\omega t$ on H. The magnetic field at any time can be written as $H_0 + h_0\cos\omega t$. Upon substituting this value of the field into (II-24) and using the criteria that $h_0 << H$, the magnetization can be written in the form

$$M_r = A_r(H,T)\left[\sin\left(\frac{2\pi F_r}{H} - 2\pi r\gamma \mp \frac{\pi}{4}\right)\cos(a\cos\omega t)\right.$$
$$\left. - \cos\left(\frac{2\pi F_r}{H} - 2r\gamma \mp \frac{\pi}{4}\right)\sin(a\cos\omega t)\right] \qquad \text{(III-7)}$$

where $a = 2\pi F_r h_0/H^2$ and $A_r(H,T)$ includes all the terms in the amplitude of the rth harmonic of (II-24).

Equation (III-7) can be expanded into harmonic components of ω in terms of Bessel functions (Goldstein et al, 1965). The time derivative of magnetization is given by

$$\frac{dM_r}{dt} = A_r(H,T) \sum_{n=1}^{\infty} (2n\omega J_n(a) \sin(n\omega t + \frac{n\pi}{2}) \sin(\frac{2\pi F_r}{H} - 2\pi r\gamma \mp \frac{\pi}{4} + \frac{n\pi}{2}) \quad \text{(III-8)}$$

where $J_n(a)$ is the Bessel function of order n. As the field H changes, each dHvA frequency term F_r generates a series of harmonics.

The dHvA signals were detected at the second harmonic of 517 Hz, which was low enough to allow complete penetration of the modulation field into the sample. If this were not the case, the Bessel function in expression (III-10) would not have the same value in all parts of the sample.

A 5.5 tesla Westinghouse superconducting magnet was used to provide the D.C. field. The dHvA frequencies were measured in the frequency range 2.7-5.5 tesla. The single crystal used in this experiment was approximately cubic in shape with a side dimension of 1 mm. All the experiments were carried out at 1.3 K. Data were collected on magnetic tape and Fourier analyzed by computer. The amplitude of each frequency was found from the Fourier transform amplitude.

The dHvA frequencies in ReO_3 were measured as a function of pressure up to 5 kbar. In addition, the pressure dependence of the Dingle temperature and the g-factor of ReO_3 along the [111] direction were measured.

The Dingle temperature was found from the variation of the dHvA amplitude with magnetic field, knowing the cyclotron mass from previous measurements (Razavi and Datars, 1976).

The ratio of the fundamental amplitude to the second harmonics (Shoenberg-Vuillemin, 1966 , Randles, 1972) was used for measuring the g factor. From (II-24) this ratio is

$$\frac{A_1}{A_2} = \sqrt{2}\, e^{\alpha m^* T_D/H} \frac{\sinh(2\alpha m^* T/H)}{\sinh(\alpha m^* T/H)} \cdot \frac{\cos\pi s}{\cos 2\pi s} \cdot \qquad \text{(III-9)}$$

where $s = \frac{1}{2} g m^*$. In the field modulation technique, the ratio of the observed dHvA amplitudes must be corrected for the factor $J_2 (\frac{2\pi F h_0}{H^2}) / J_2 (\frac{4\pi F h_0}{H^2})$. From the measurement of A_2/A_1, m^*, and T_D the value of $G = \frac{\cos\pi s}{\cos 2\pi s}$ and thus s can be computed.

Fig. 5 shows the variation of G as a function of s. It is clear that all the solutions of the form $n \pm s$, where n is an integer, are possible if the sign of $\cos\pi s$ is not known. The sign of $\cos\pi s$ can be determined by an absolute phase measurement (Coleridge and Templeton, 1972). Knowing the sign of $\cos\pi s$ allows the determination of $2n \pm s$.

The observed amplitudes can differ from the ideal Lifshitz-Kosevich (LK) amplitude because of magnetic interaction (MI) effects (Shoenberg, 1962). The MI effect arises because the electrons see the total magnetic induction $B = H + 4\pi M$ rather than the applied field H alone. Therefore, the (LK) relation is modified to

$$M = \sum_{r=1}^{\infty} A_r \sin[2\pi r(\frac{F}{4\pi M + H} - \gamma) \mp \frac{\pi}{4}] \qquad \text{(III-10)}$$

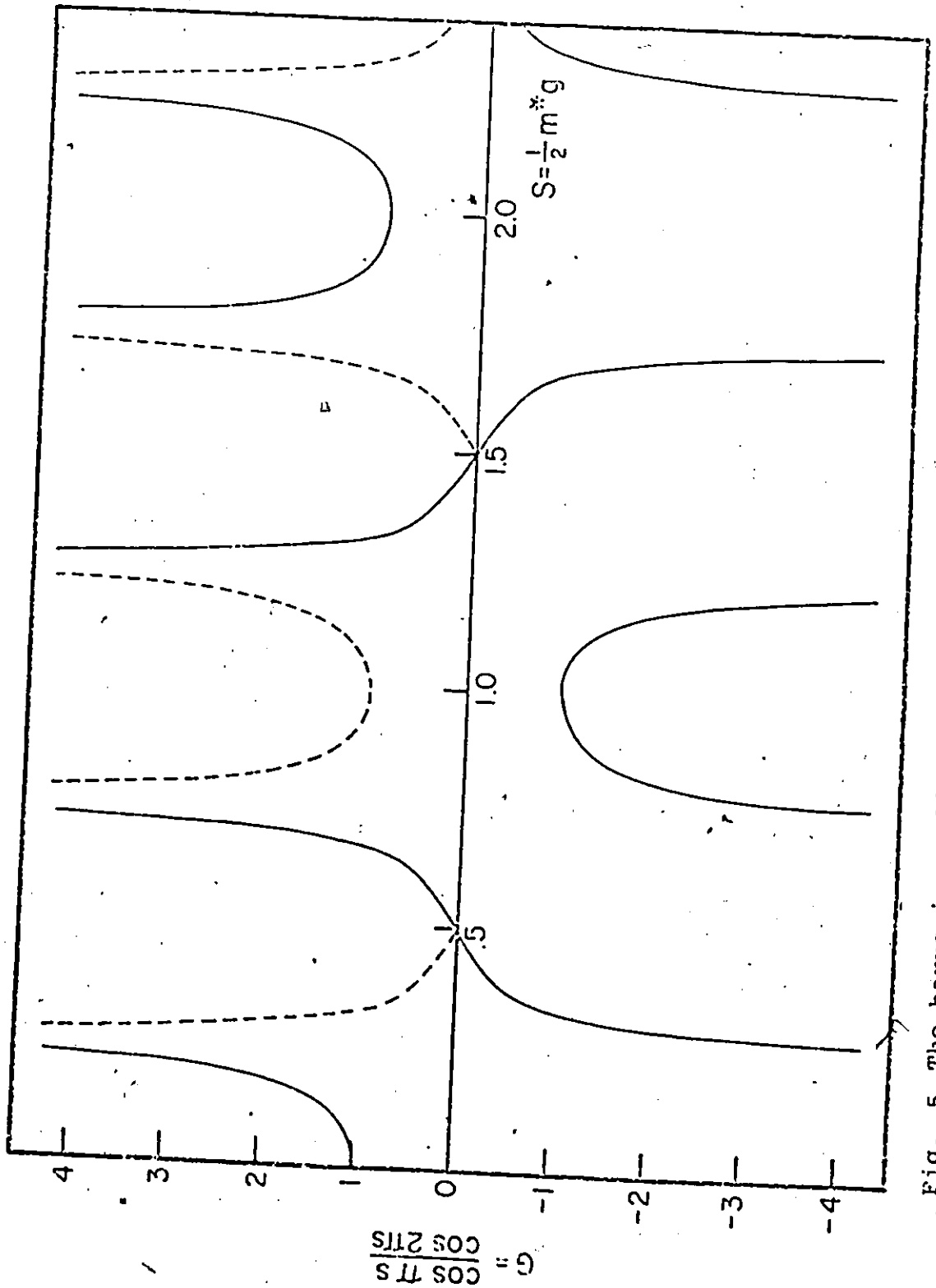

Fig. 5 The harmonic amplitude ratio, G, as a function of $S = \frac{1}{2} m^*g$

where $A_r = \frac{DB^{1/2}}{r^{3/2}} I_r k_r \cos(\pi rs)$. Since $4\pi M << H$, the substitution of H by B has a minute effect on the slowly-varying amplitude A_r, however, the argument of the sin term changes rapidly.

Phillips and Gold (1969) have obtained an approximate solution of equation (III-10) for a weak interaction. The result for the first three harmonics is given by

$$\begin{aligned} M = {} & A_1 \sin(x + \psi_1) \\ & + A_2\{\sin(2x + \psi_2) - \tfrac{1}{2}\nu \sin(2x + 2\psi_1)\} \\ & + A_3[\sin(3x + \psi_3) - \tfrac{3}{2}\alpha\nu[\sin(3x + \psi_1 + \psi_2) \\ & - \tfrac{1}{4}\nu \sin(3x + 3\psi_1)]\} \end{aligned}$$

where $x = 2\pi\left(\frac{F}{H} - \gamma\right)$ and $\nu = k\frac{A_1^2}{A_2}$. Therefore, for the weak interaction, the fundamental amplitude is unchanged, but the second and the third harmonic differ in amplitude and phase from the ideal LK values.

By simple analysis Randles (1972) and Alles et al (1975) have obtained the LK amplitudes in terms of the observed amplitudes and the relative phase factor

$$\begin{aligned} A_1 &= A_1' \\ A_2 &= \sqrt{2}A_2' \cos(2\phi_1 - \phi_2) \end{aligned} \qquad \text{(III-12)}$$

where A_1', ϕ_1 and A_2', ϕ_2 are the observed amplitude and phase of fundamental and the second harmonic, respectively.

Using the above relations in (III-9) an expression for the function $G = \frac{\cos\pi s}{\cos 2\pi s}$ is found to be

$$G = \frac{A_1'}{2A_2' \cos(2\phi_1 - \phi_2)} \frac{J_2(4\pi Fh_0/H_2)}{J_2(2\pi Fh_0/H^2)} * \frac{\sinh(\alpha m^* T/H)}{\sinh(2\alpha m^* T/H)} * e^{-\alpha m^* T_D/H} \quad \text{(III-13)}$$

In ReO_3 the magnetic interaction is weak since KA_1 for the α frequency along [111] direction is about .01. Thus it is appropriate to use eq. (III-13) for calculating g-factors.

d. High Pressure System

This section is divided into three parts as follows:

1. A description of the high pressure apparatus.
2. The dHvA pressure cell, the dHvA coil and the electrical feedthrough.
3. The procedure for obtaining hydrostatic pressure at liquid helium temperatures.

1. Description of the high pressure apparatus

High pressures up to 5 kbar were obtained using a modified Harwood Engineering Portable Pressure Generating system. The system includes a two stage gas compressor to take helium up to 7 kbar at room temperature. Fig. 6 shows schematically the high pressure apparatus (Slavin and Datars, 1974).

A charge pressure (minimum .07 kbar) is produced by a commercially bottled supply of helium gas. The air compressor provides a continuous air pressure at the air-to-oil booster pump (P-1). The oil pressure can be pumped to a maximum of

1.38 kbar. At this state the 1/1 gas to oil intensifier (INT-1) transmits the oil pressure to the charge gas supply. In the second stage a 14.5/1 gas to oil intensifier (INT-2) increases the helium gas pressure. The maximum pressure allowed by the system is 7 kbar.

The apparatus is equipped with several pressure gauges, GH is provided to read the helium supply pressure, G1 to read the oil pressure and MG a manganin cell to measure the high pressure. The caption of Fig. 6 gives information about the other parts used in the pressure apparatus.

A flexible 3.2 mm (.5 mm i.d.) tube was used for transmitting pressure to the pressure cell.

2. The dHvA pressure cell, the dHvA coil and the electrical feedthrough

The dHvA pressure cell was made of beryllium copper heat treated (2 hrs and 25 minutes at 315°C) to a Rockwell hardness of RC 42. Fig. 7 shows a schematic view of the dHvA pressure cell.

The modulation coil consists of two layers of #34 nyclad wire, total of 260 turns, wound on the exterior of the pressure cell Fig. 7. The dHvA detection coils consist of a pick up and balance coil, each having 578 turns of #40 nyclad wire, wound directly on the sample holder.

The sample holder was made of G10 fiber glass epoxy and was cylindrical in shape (3 cm height and .925 cm diameter).

Key to Fig. 6

 manually operated needle valve

 filter

 pressure gauge

 check valve:

 pressure release rupture valve

FH - oil filter

AS - air supply

FA - air filter

AR - air regulator

GA - air pressure gauge

AT - air throttle used to regulate pumping rate of intensifier

P1 - air-to-oil booster pump

G1 - oil Heise gauge on front panel

GH - helium pressure gauge at the helium cylinder

MG - manganin pressure gauge

INT.1 One-to-one oil to gas intensifier

INT.2 14.5 to 1 oil to gas intensifier

SV - High pressure safety valve.

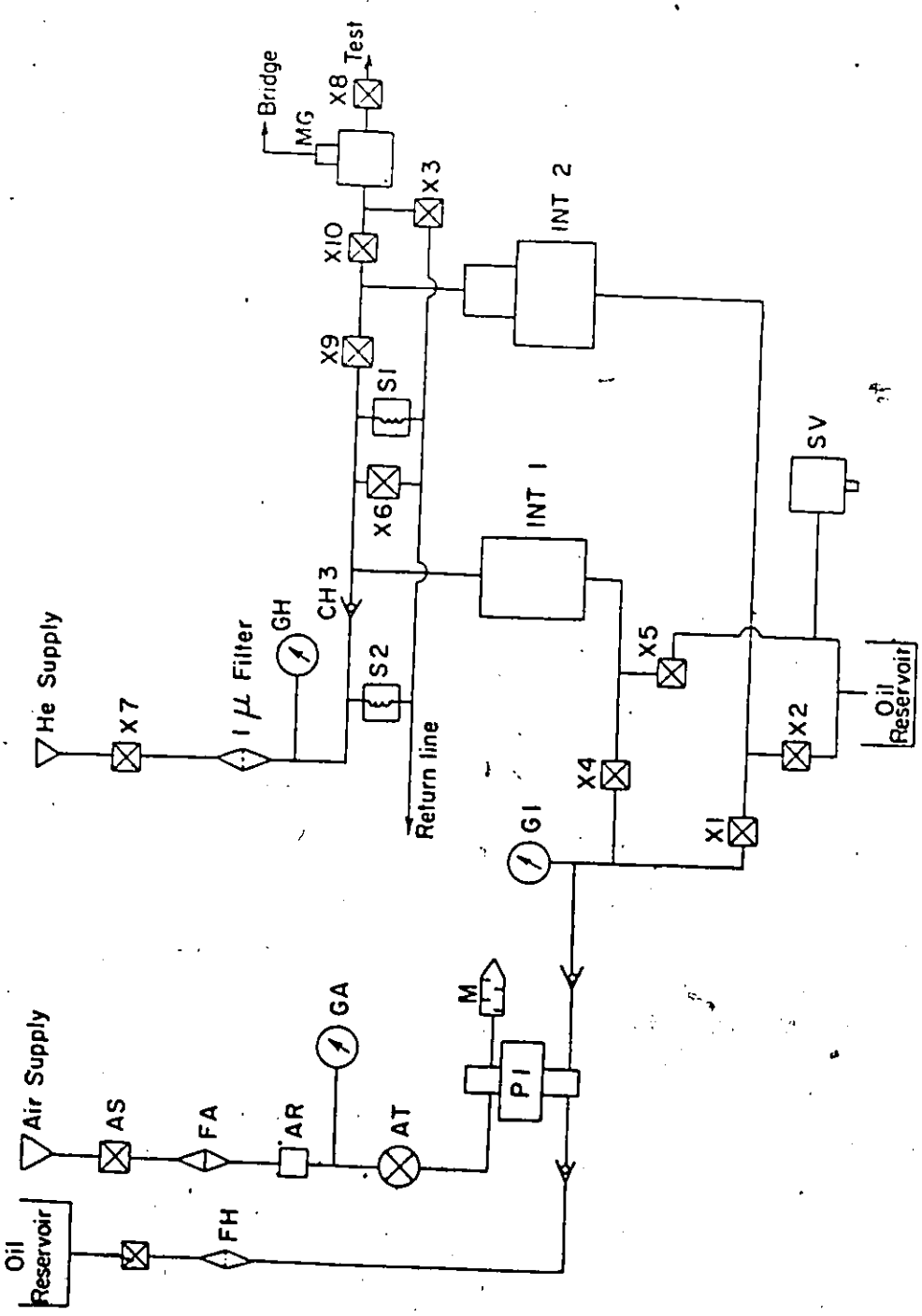

Figure 6

Block diagram for the high pressure system.

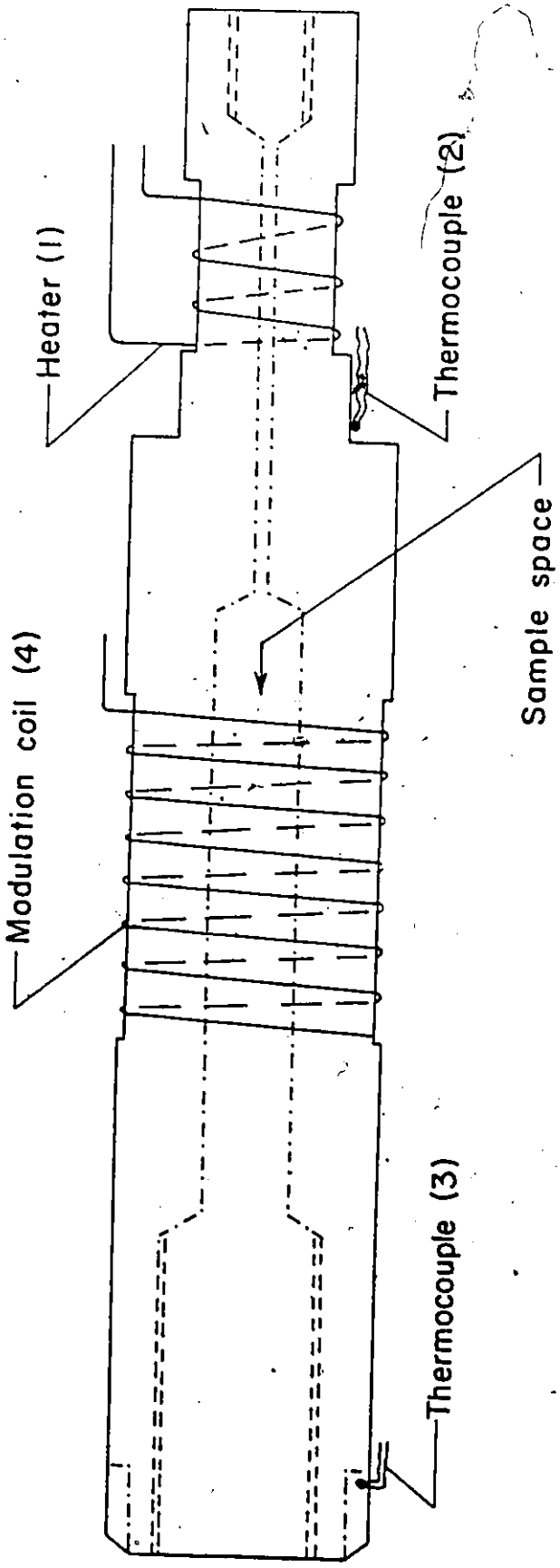

Figure 7

Schematic diagram of the high pressure electrical feedthrough and dHvA pick up coil.

The plug and electrical feedthrough assembly shown in Fig. 8 were made of 316 stainless steel (Schirber, Shanfeldt, 1968). The plug was cut so that a high pressure seal was obtained by tightening the BeCu screw. A kel-F washer was used for insulating the electrical feedthrough from the plug. The kel-F washer also acted as a high pressure seal. At a pressure above .7 kbar the piston pushed the washer, the washer expanded and made the proper seal. Unfortunately, this type of seal leaks at pressures lower than .7 kbar and the system must be pressurized first at room temperature for proper sealing.

3. Procedure for obtaining hydrostatic pressure at liquid helium temperature

All the dHvA experiments were carried out at 1.3 K. At this temperature the helium gas solidifies at pressures above 25 bars. Thus, solid helium was used as the transmitting medium of pressure on the sample. The freezing of helium was carried out at a constant pressure p_m for which there was a freezing temperature T_m, Fig. 9 (Spain and Segall, 1971). Helium was solidified slowly from the bottom of the pressure cell toward the capillary inlet at the top to obtain hydrostatic pressure. To do this, a temperature gradient (about 3°C) was produced between the bottom of the pressure cell and the capillary inlet at the top. This condition was ensured by heating the top of the cell while transferring cold helium gas to the bottom. The temperatures were monitored at both ends

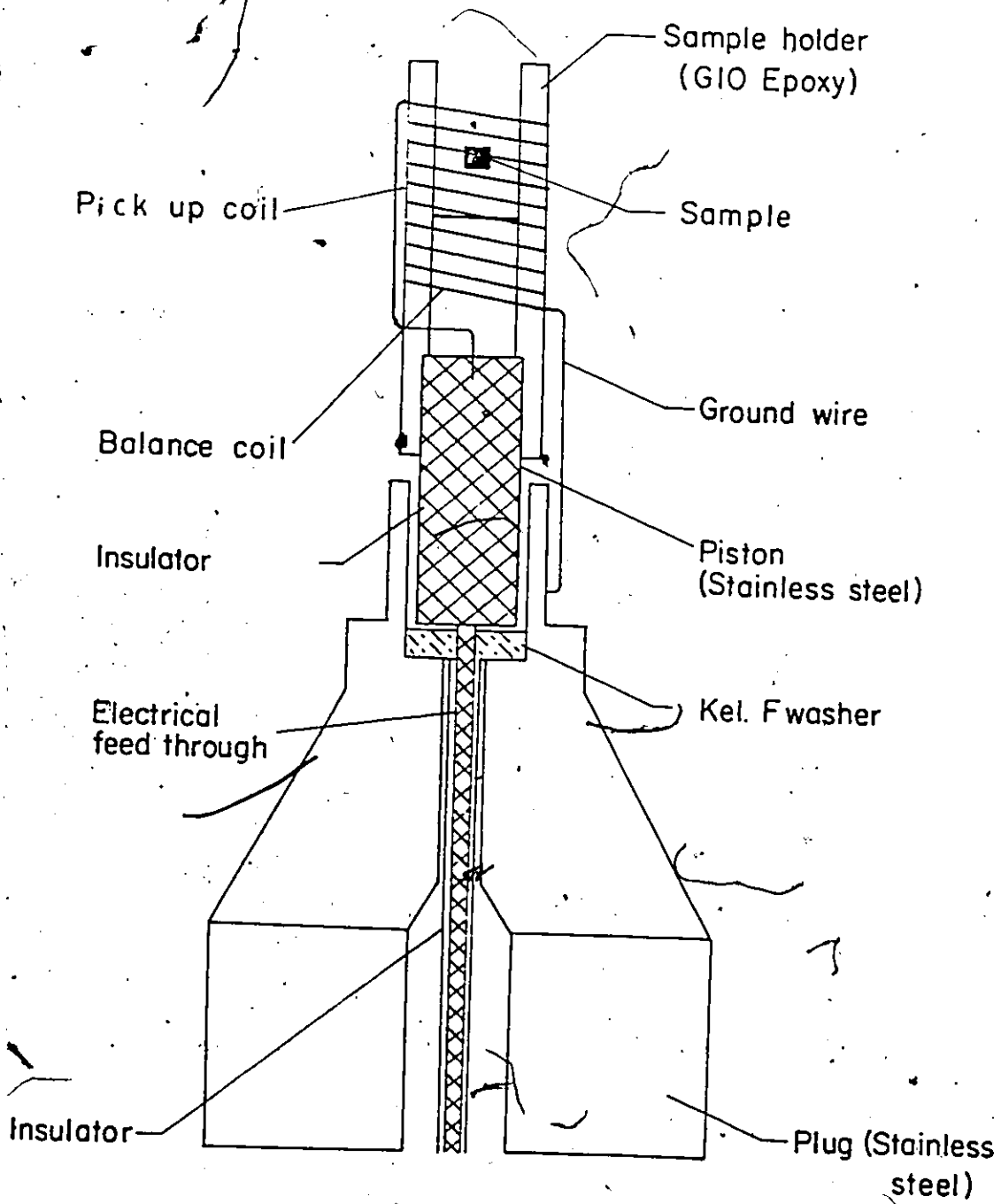

Figure 8

Schematic diagram of high pressure electrical feedthrough and dHvA pick up coil.

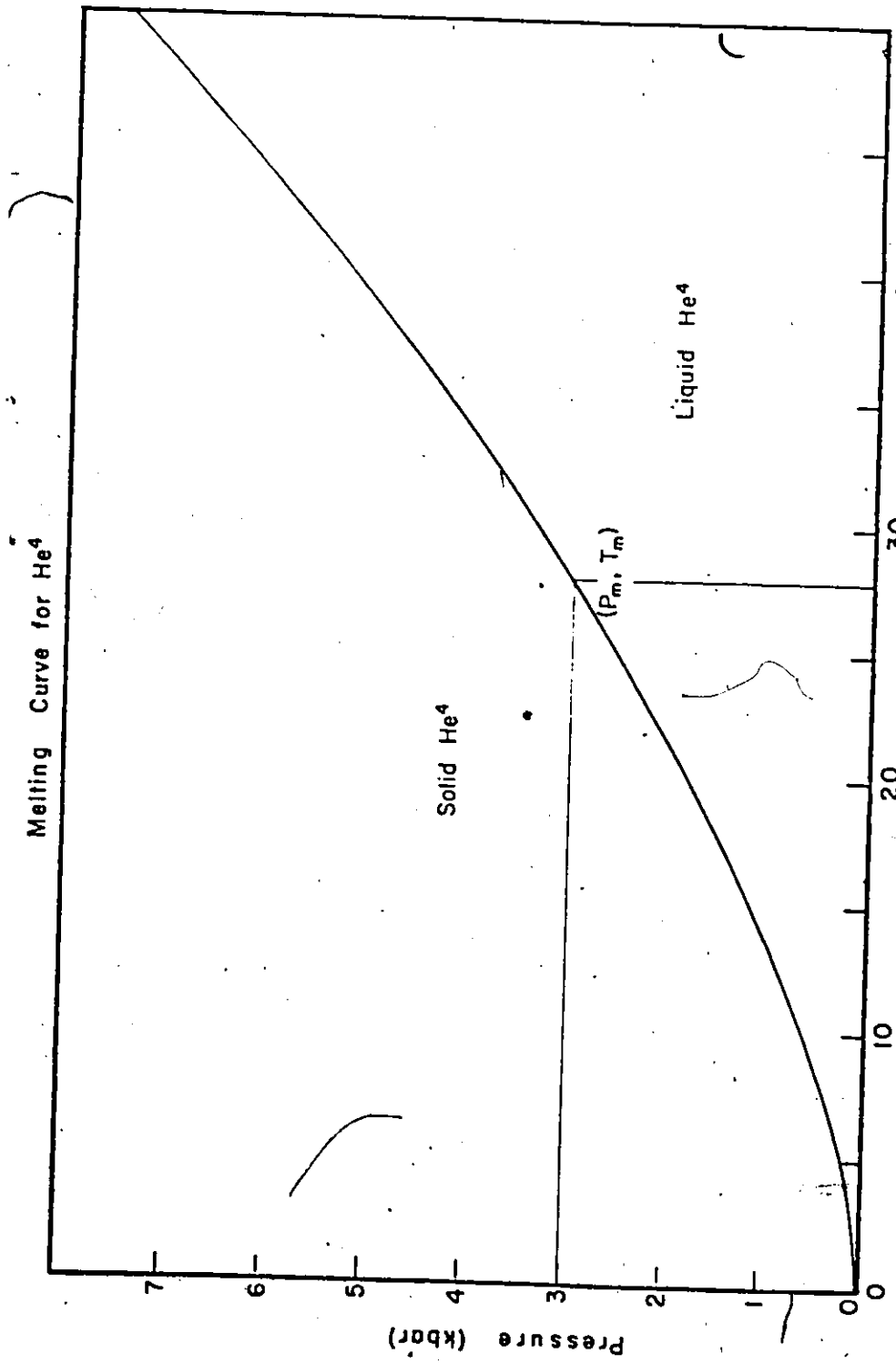

P-T diagram for He^4.
Figure 9

of the pressure cell by two copper constantan thermocouples, and pressure p_m at freezing was read by the manganin resistance gauge (MG). The manganin gauge was calibrated by Harwood Engineering.

The pressure dependence of the superconducting transition temperature, T_c, of tin was employed in order to obtain a relationship between the pressure of solid helium in the cell and the pressure gauge reading. The slope $\frac{dT_c}{dp}$ in this region of pressure (up to 5 kbar) was in agreement with previous work (Jennings and Swenson, 1958). This result set the uncertainty in the pressure reading to 1%. Therefore, it was not necessary to include corrections due to the contraction of solid helium on cooling.

e. Method of Measuring the Electrical Resistivity at High Pressure

To study the effect of pressure on the resistivity of ReO_3, the Montgomery four-probe method (Montgomery, 1971) was used. In this method, a single crystal sample is cut in the form of a rectangular prism with small electrodes attached at four corners. By passing a small current I_1 through two electrodes and measuring the voltage across the other two electrodes the resistivity ρ of the sample is obtained. For the crystal with the dimension ℓ_1, ℓ_2 and ℓ_3 the resistivity is

$$\rho = HE \frac{V_1}{I_1} \qquad \text{(III-14)}$$

where H is a function of ℓ_2/ℓ_1 and E is an effective thickness depending on ℓ_3 (Logan et al, 1971). The pressure dependence

of the resistivity (ρ) of ReO_3 was measured at several temperatures. The temperature was measured by a copper-constantan thermocouple. The sample was a rectangular prism with dimensions 1.9×1.7×.8 mm. With these dimensions, the geometrical factor HE had a value of .64.

It was not possible to solder the electrodes on the sample since the sample decomposed with heat or alloyed with the solder material. The contacts were, therefore, spring loaded to the sample. Four springs of copper bronze made contacts at four corners of the sample. The sample was glued to the sample holder in order to prevent any movement. A schematic diagram of the sample holder is shown in Fig. 10. The dHvA pressure cell was used to measure the resistivity under pressure. A stainless steel electrical feedthrough assembly with three leads was used. The electrical measurements were made in an A.C. mode. Alternating current with a frequency of approximately 0.1 Hz was passed through the sample between two current probes. A synchronized very low frequency phase detection system was used to amplify the voltage between two potential probes and to obtain the in phase component of the signal.

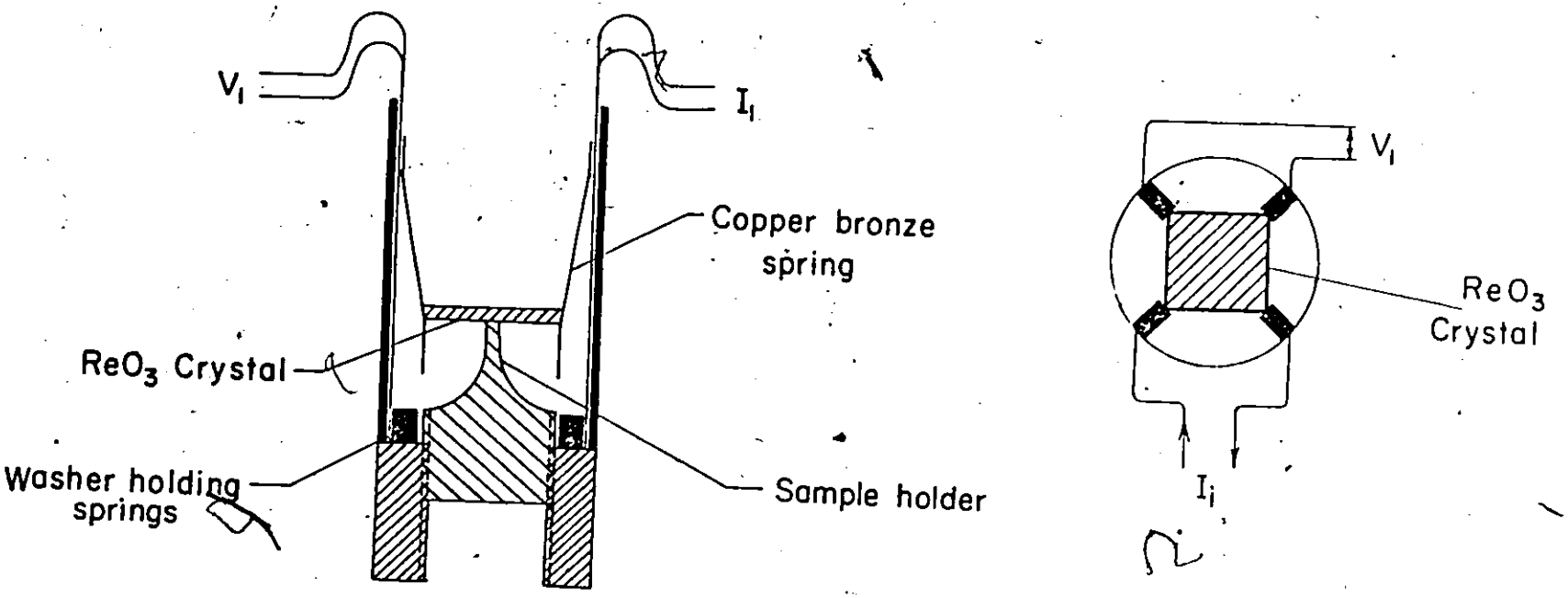

Figure 10

Schematic diagram of the sample holder for the resistivity measurements of ReO_3 at high pressure.

CHAPTER IV

RESULTS AND DISCUSSION OF INDUCED TORQUE IN ReO_3

Induced torque in different crystallographic planes was studied by orienting the ReO_3 crystal in 5° intervals about the [110] direction. Fig. 1[illegible] shows an example of induced torque for rotation in a plane tilted 40° from the [110] direction. A precise orientation of the plane of rotation is needed to plot the stereographic projection of the open orbit direction. The uncertainty, more than ±2°, was found in the reading of the screwdriver rotation used for changing the planes of rotation by 5°. To overcome this problem, the positions of the <110> and <010> open orbit peaks were used as reference points. To check this procedure, the orientation of the plane of rotation of Fig. 11 was also determined from the frequencies of dHvA oscillations that were detected as a function of magnetic field strength. The orientation obtained from both results agrees to within ±1°.

The stereographic projection of the magnetic field directions in which open orbit peaks were observed are shown in Fig. 12. The open orbit directions are perpendicular to the planes in which the open orbit peaks were observed. The plane in which the magnetic field was rotated for Fig. 11 is shown

Figure 11

An induced torque rotation diagram for a plane tilted 40° from the [001] direction about [110]. The magnetic field is parallel to the [110] direction at the <100> open orbit peaks and angle markers are shown at 10° intervals. The data were obtained in a magnetic field of 5.4 T. The direction of the open orbits giving rise to the peaks are specified.

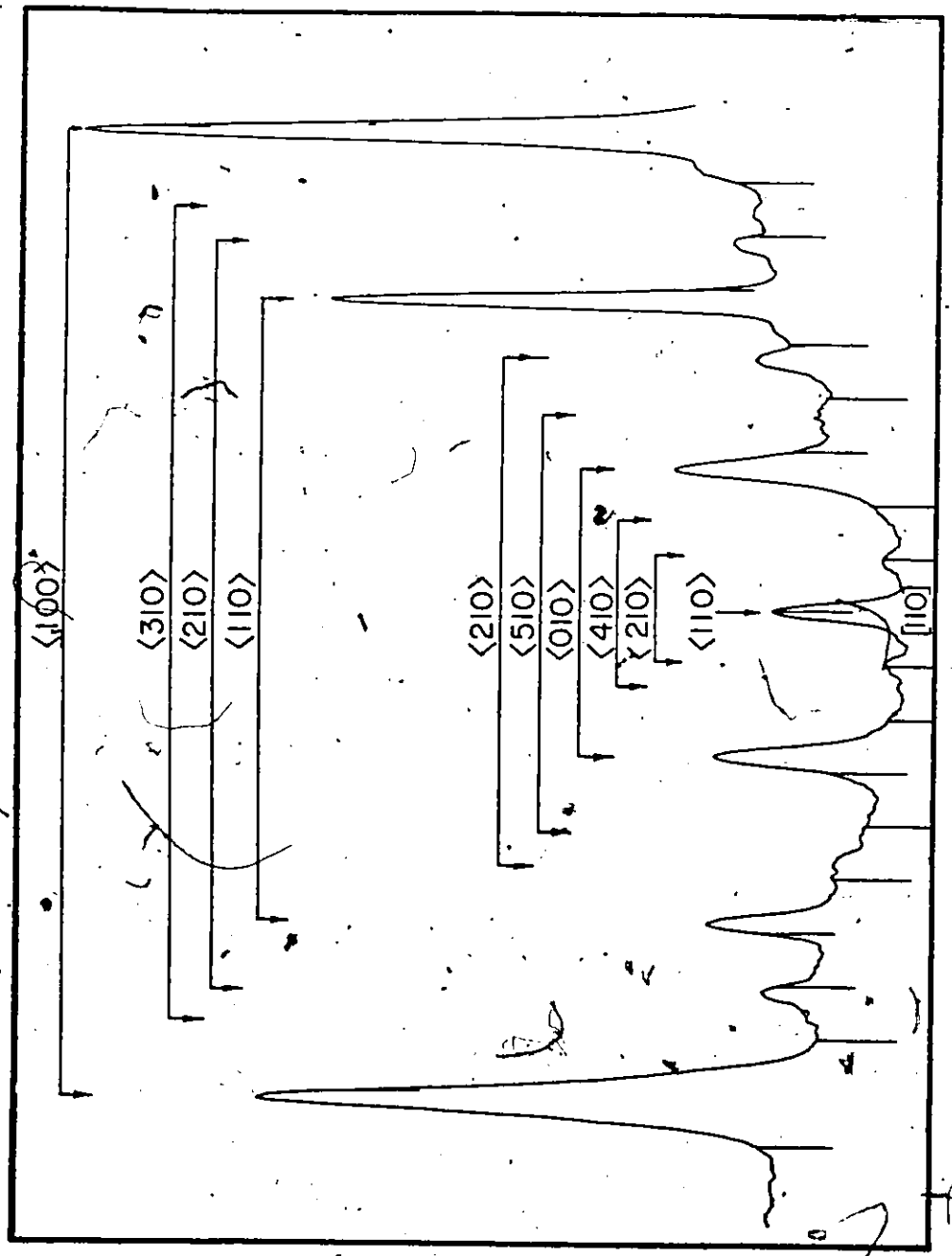
INDUCED TORQUE (arbitrary units)
FIELD DIRECTION
⟨001⟩
⟨310⟩
⟨210⟩
⟨110⟩
⟨210⟩
⟨510⟩
⟨010⟩
⟨410⟩
⟨210⟩
⟨110⟩
[110]

with a dashed line in Fig. 12.

The [100] and [010] open orbits are primary open orbits running along tubes of the connected γ Fermi surface. The [100] peak is larger than the [010] peak in Fig. 11 because only the [100] open orbit is 90° from the torque direction which gives the maximum torque amplitude. Secondary open orbits are along <110> directions. Higher-order open orbits evident in Fig. 11 and Fig. 12 are along <210>, <310>, <410> and <510> directions. Higher open directions such as <610>, <710> ··· are also observed; in Fig. 11, the small peak on the shoulder of the [100] open orbit peak, corresponds to one of the higher open orbit directions. The higher open orbit direction in Fig. 12 appears as a series of points close to the $[\bar{1}10]$ pole. The difference in amplitude of induced torque peaks for the same type of open orbit at symmetry related directions in Fig. 11 is due to the fact that the plane of rotation was 6° from a plane with mirror symmetry and to the non spherical shape of the sample.

To study the amplitude of open orbit torque, the background torque was subtracted from the open orbit peaks. This caused a relative error of 5% in determining the open orbit torque amplitude.

A log-log plot of field dependence of the torque amplitude for primary, secondary and tertiary open orbits is shown in Fig. 13. The field dependence shows quadratic ($N \propto H^{1.97}$) behaviour for the [100] primary orbit whereas the [010] peak

Figure 12

Stereogram of magnetic field directions along which open-orbit peaks have been observed. The dashed line shows how the example data trace of Fig. 11 is plotted on the diagram.

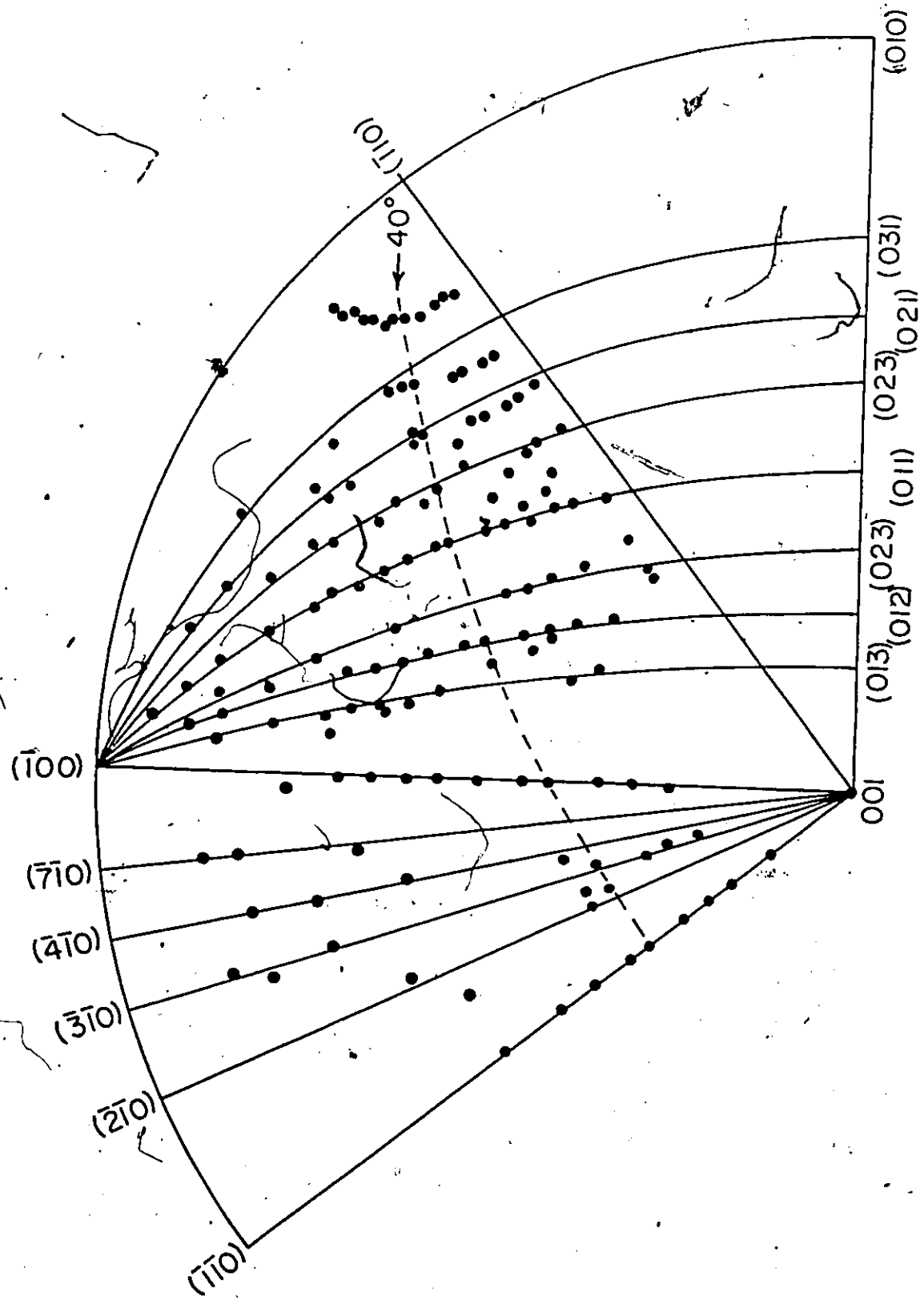
(010)
(011)
40°
(031)
(021)
(023)
(011)
(012)
(023)
(013)
001
100
(1̄00)
(7̄1̄0)
(4̄1̄0)
(3̄1̄0)
(2̄1̄0)
(1̄1̄0)

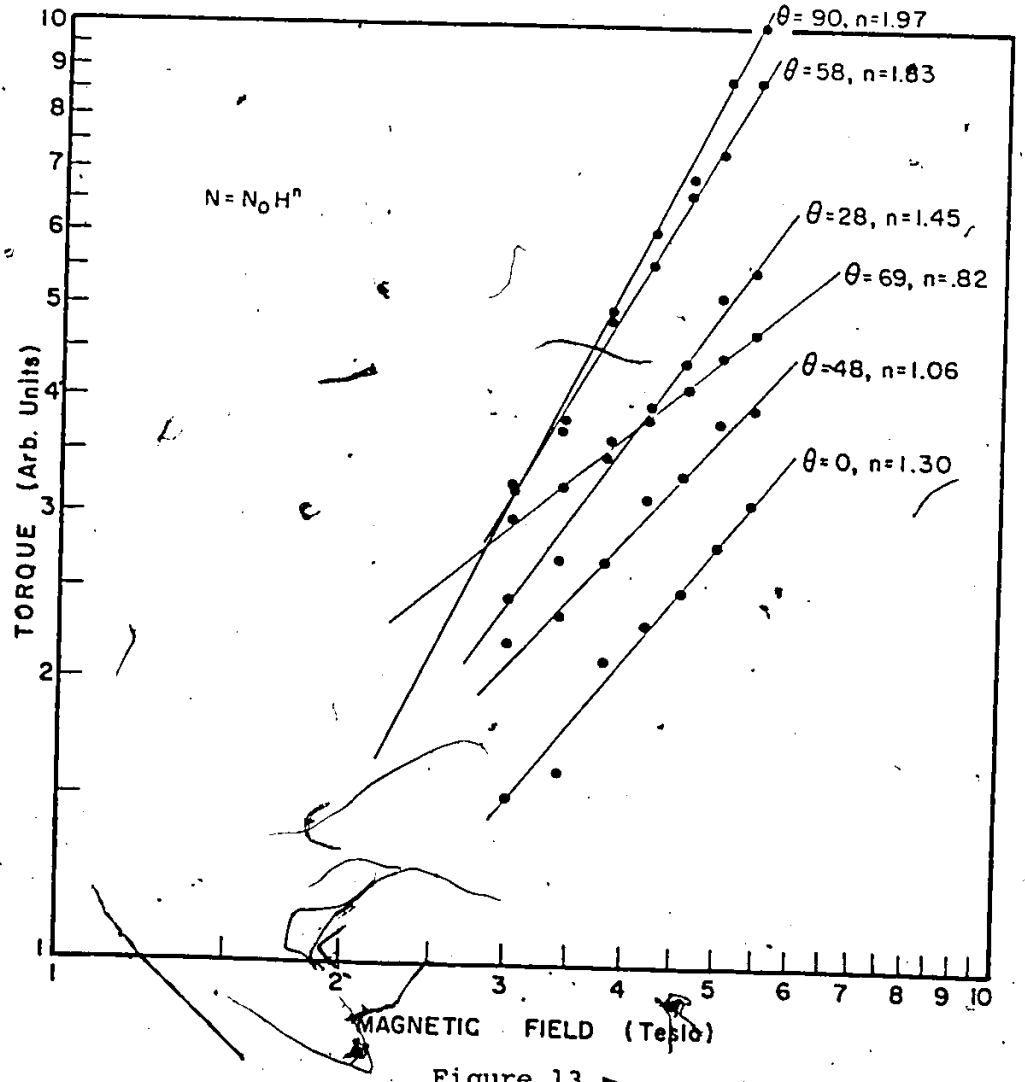

Figure 13

Log-log plot of the field dependence of induced torque amplitude of several observation directions of Fig. 1. The dependence approximates B^n for most directions ($n = 1.00 \rightarrow 2.04$).

has the value of 1.45 for the field exponent. This indicates that the angle between the torque axis and the open orbit direction has an effect on the field dependence of the torque amplitude. The field dependence of torque amplitude of secondary and tertiary open orbits also deviates from quadratic behaviour.

It was shown in chapter III-a that, in high field limit, the amplitude of the torque induced by an open orbit depends on the tilt angle α between the open orbit direction and the x-axis. For magnetic field directions in the $(\bar{1}\bar{1}0)$ plane, the amplitude of the primary <100> open orbit was maximum and decreased by changing the plane of rotation. The tilt angle α is defined with respect to the plane of rotation in the Fig. 14. Figure 14 also shows dependence of the primary torque amplitude on α. It exhibits a smooth geometric dependence as a function of α. The data of Fig. 14 were fitted to $A\cos^2\alpha$. The fitted and experimental results are in good agreement and the slight discrepancy between the calculated and experimental results is due to 5% error in determination of the torque amplitude. In the $(\bar{1}00)$ plane the primary open orbit was not observed because the torque observation axis and the primary open orbit coincide.

The theoretical calculation of Mattheiss (1969) for ReO_3 suggests open orbits along <100> in the third band (γ Fermi surface, Fig. 2). The γ Fermi surface sheet is similar

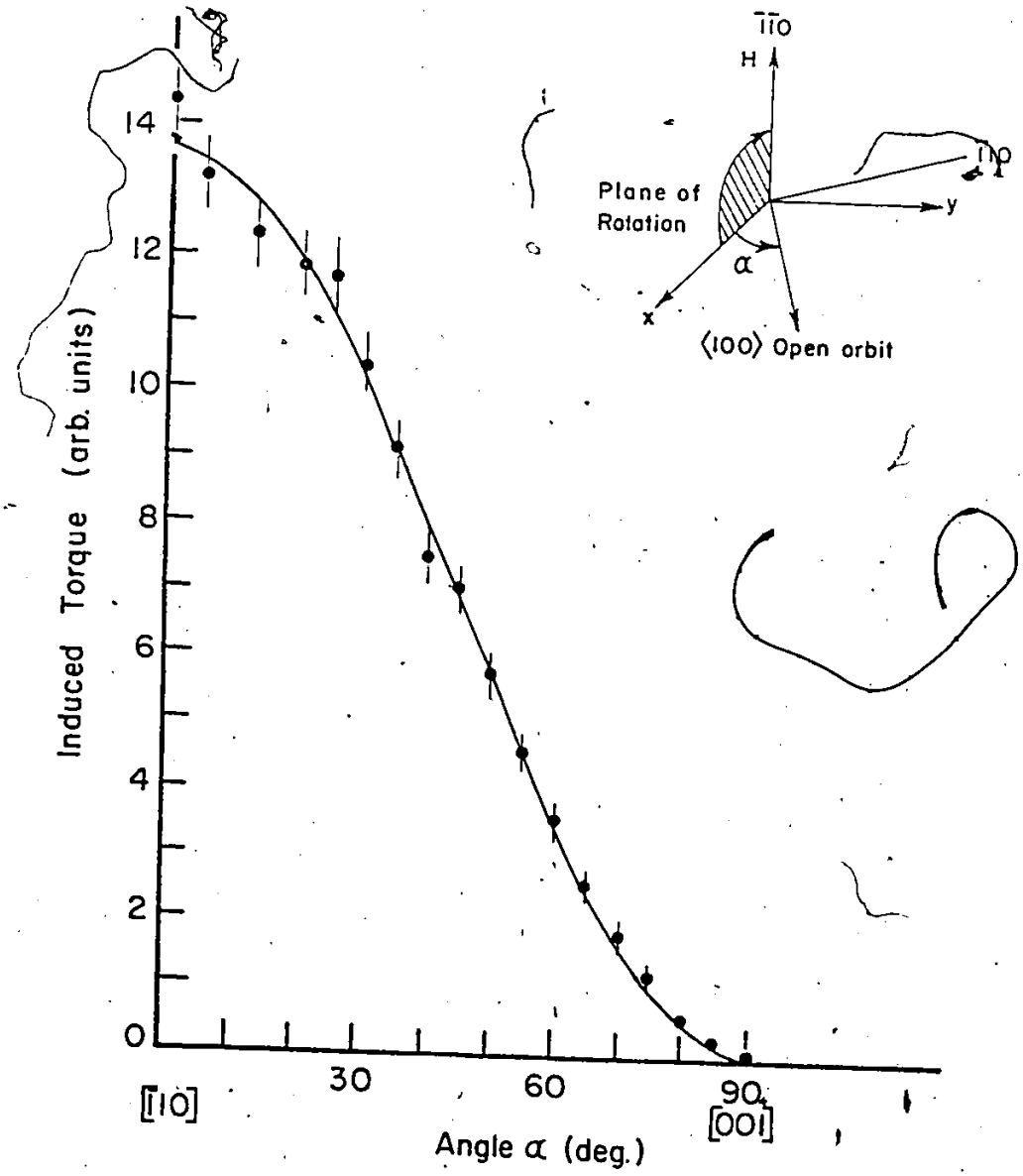

Figure 14

Angular dependence of primary open orbit torque amplitude at constant field of 5.4 T. The angle of the plane of rotation is indicated at the top of the figure.

to the three-dimensional grid used by Lifshitz and Peschanskii (1959) (Fig. 1) for investigating the galvanomagnetic properties of metals with this type of Fermi surface and determining the characteristic of the angular dependence of these properties. The open orbit directions in ReO_3 obtained from the torque experiments agree with predictions of Lifshitz and Peschanskii (1959) for the Fermi surface similar to the γ Fermi surface sheet. The open orbit directions in ReO_3 also support the APW calculation of Mattheiss (1969).

The torque results also provide information about the effective conductivity tensor as was noted in III-b. Using III-2 and approximating the sample as a sphere of radius $R = 8\times10^{-4}$ m, the torque for ReO_3 can be described by

$$N_y = 1.246\times10^{-14}\ B^2\ \sigma^* \ .$$

Table 3 shows the torque for the [100] primary open orbit as well as the value for the conductivity tensor for several field values. The result indicates that the effective conductivity tensor is constant for all field values

$$\bar{\sigma}_{xx} = 1.45\times10^{11}\ (\text{ohm.m})^{-1} \ .$$

This also indicates that the data were taken in the high field region since from III.6 the effective conductivity tensor is

$$\bar{\sigma}_{xx} = c_1 \cos^2\alpha + c_2 B^{-2}$$

Table 3. Field dependence of torque amplitude and effective conductivity

Field in Tesla	Torque Amp in Nm $\times 10^{-7}$	$\bar{\sigma}_{xx} \times 10^{11}$ $(\Omega.m)^{-1}$
4.9	4.21	1.41
4.8	4.18	1.46
4.5	3.66	1.45
4.2	3.18	1.45
3.9	2.77	1.46
3.4	2.14	1.49
3.05	1.66	1.43

For the <100> primary open orbit $\alpha = 0$ and at high field region C_2B^{-2} is small. Thus $\sigma^* = C_1$, in agreement with the experimental data.

CHAPTER V

THE EFFECT OF HIGH PRESSURE ON THE FERMI SURFACE, DINGLE TEMPERATURE, g FACTOR AND RESISTIVITY OF ReO_3

a - Result:

The pressure dependence of the dHvA frequencies in ReO_3 single crystal was measured, with the magnetic field along the [111] and [001] directions. These two symmetry directions were chosen because four frequencies are well separated along the [001] direction and the amplitude of the α frequency is dominant along the [111] direction. The experiment was repeated eight times along the [111] direction with pressures up to 5 kbar to check the reproducibility of the results. In three experiments, the γ_1 frequency was detected which indicated that the orientation was in error by more than 5 degrees from the [111] direction. These data were not included in the analysis. For the remaining five experiments with a [111] sample orientation, the measured α frequencies were grouped and averaged over ±.1 kbar of pressure. Along the [001] direction, Fig. 3 shows that there are three electron-like orbits α, β and γ_1 and a hole-like orbit γ_2. Frequencies along the [001] direction were averaged in a similar way to those along the [111] direction.

Fig. 15 shows the pressure dependence of the α frequency for both the [001] and [111] magnetic field directions. The α

Figure 15

Pressure dependence of the α frequency of ReO_3 for the magnetic field parallel to the [111] and [001] directions. The frequency scales for the [111] and [001] directions are on the left and right sides, respectively.

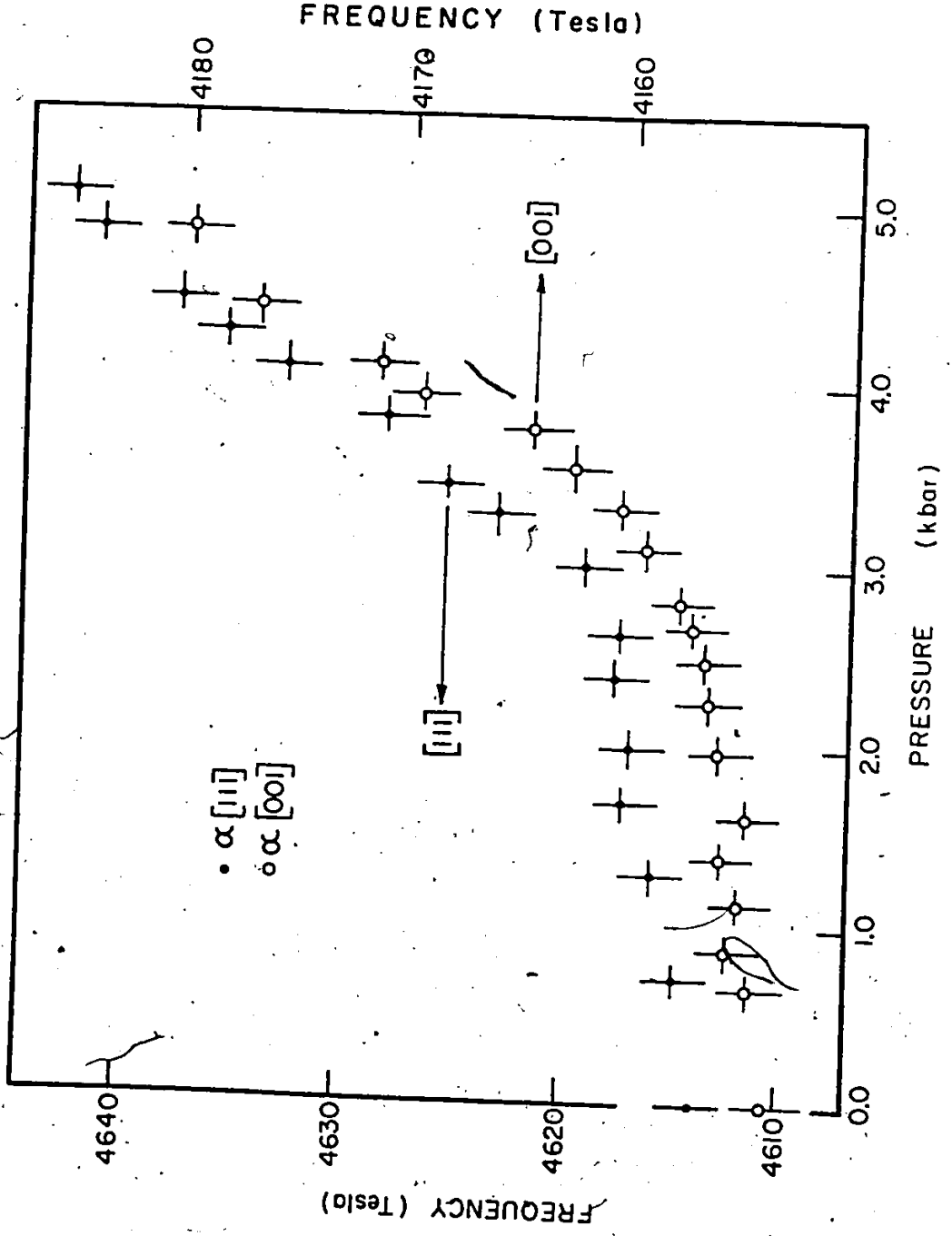
FREQUENCY (Tesla)
4180
4170
4160
[001]
[111]
• α [111]
○ α [001]
PRESSURE (kbar)
5.0
4.0
3.0
2.0
1.0
0.0
4640
4630
4620
4610
FREQUENCY (Tesla)

frequency for both directions increases linearly with pressure up to 3 kbar and then increases at a faster rate with pressure up to 5 kbar.

Fig. 16 shows the pressure dependence of the β, γ_1 and γ_2 frequencies with the magnetic field along the [001] direction. The β and γ_1 frequencies increase linearly with pressure up to 1.4 kbar, and then do not change appreciably between 1.4 and 2.4 kbar. Above 2.4 kbar, however, both frequencies show a large increase with pressure similar to that of the α frequency at high pressures. The change with pressure for the hole-like orbit γ_2 is small up to 3 kbar and is large above 3 kbar. The relative change in frequencies between 2.4 and 5 kbar is about 0.55% for the α and γ_2 frequencies and 0.45% for the β and γ_1 frequencies.

The horizontal error bars in Figs. 15 and 16 represent the range of pressure of ±.1 kbar over which measurements were averaged. The vertical error bars are due to uncertainty in the value of frequency obtained from the Fourier transform of the computer analyses of the data points. The uncertainty of 1.5 to 2.5 T was the half width of peaks of the Fourier transform of the dHvA oscillations. Table IV shows the α, β, γ_1 and γ_2 frequencies between 0 and 5.06 kbar for the [001] and [111] directions.

The initial area compressibilities (eq. II-29)

Figure 16

Pressure dependence of the β_1, γ_1 and γ_2 frequencies of ReO_3 for the magnetic field parallel to the [001] direction.

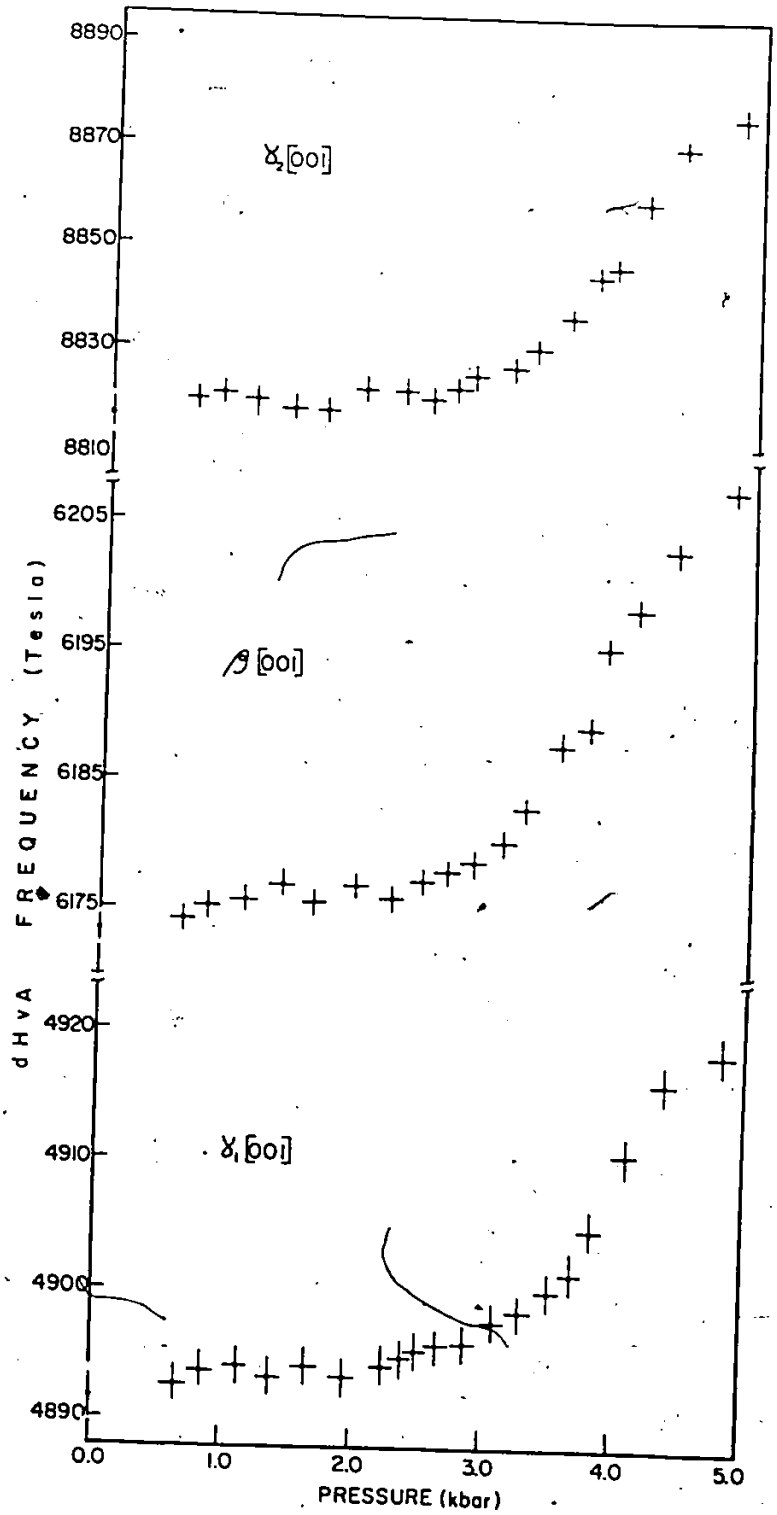
8890
8870
8850
8830
8810
6205
6195
6185
6175
4920
4910
4900
4890
dHvA FREQUENCY (Tesla)
γ2[001]
β[001]
γ1[001]
0.0
1.0
2.0
3.0
4.0
5.0
PRESSURE (kbar)

$$\frac{1}{F(0)}\left(\frac{dF(P)}{dP}\right)_{P=0} = \frac{1}{A}\frac{dA}{dP}$$

for all frequencies were calculated using a linear least squares fit to the low pressure data and are listed in Table V. The results are compared with the fluid helium phase-shift results (Schirber et al.,1972) and the predictions of a Korringa, Kohn and Rostoker (KKR) calculation (Myron et al.,1973). Table V also shows the measured area compressibilities in the high pressure region.

The Dingle temperature and the g factor were measured as a function of pressure up to 5 kbar along the [111] direction. The value of the effective mass is needed to obtain the Dingle temperature and the g-factor. Along the [111] direction at 4.32 kbar, the effective mass was found to be 0.69 which is the same as the value at zero pressure (Razavi, Datars, 1976). The error in effective mass is about 2%. The Dingle temperature was determined from a least square fit of the slope of $\ln(A\sqrt{H}\ \sinh(\alpha m^* T/H)/J_2(2\pi fh/H^2)$ vs H^{-1}. A Dingle plot for a pressure of 4.9 kbar is shown in Fig. 17 and the Dingle temperature at different pressure is shown in Fig. 18. Figure 18 shows that no significant variation of the Dingle temperature with pressure was observed. It was also found that the Dingle temperature is not the same in different experiments at a specific pressure. This was caused by variations in sample strain caused by the applied pressure and the rate of freezing of the high-pressure helium gas. Any change in the crystal strain and

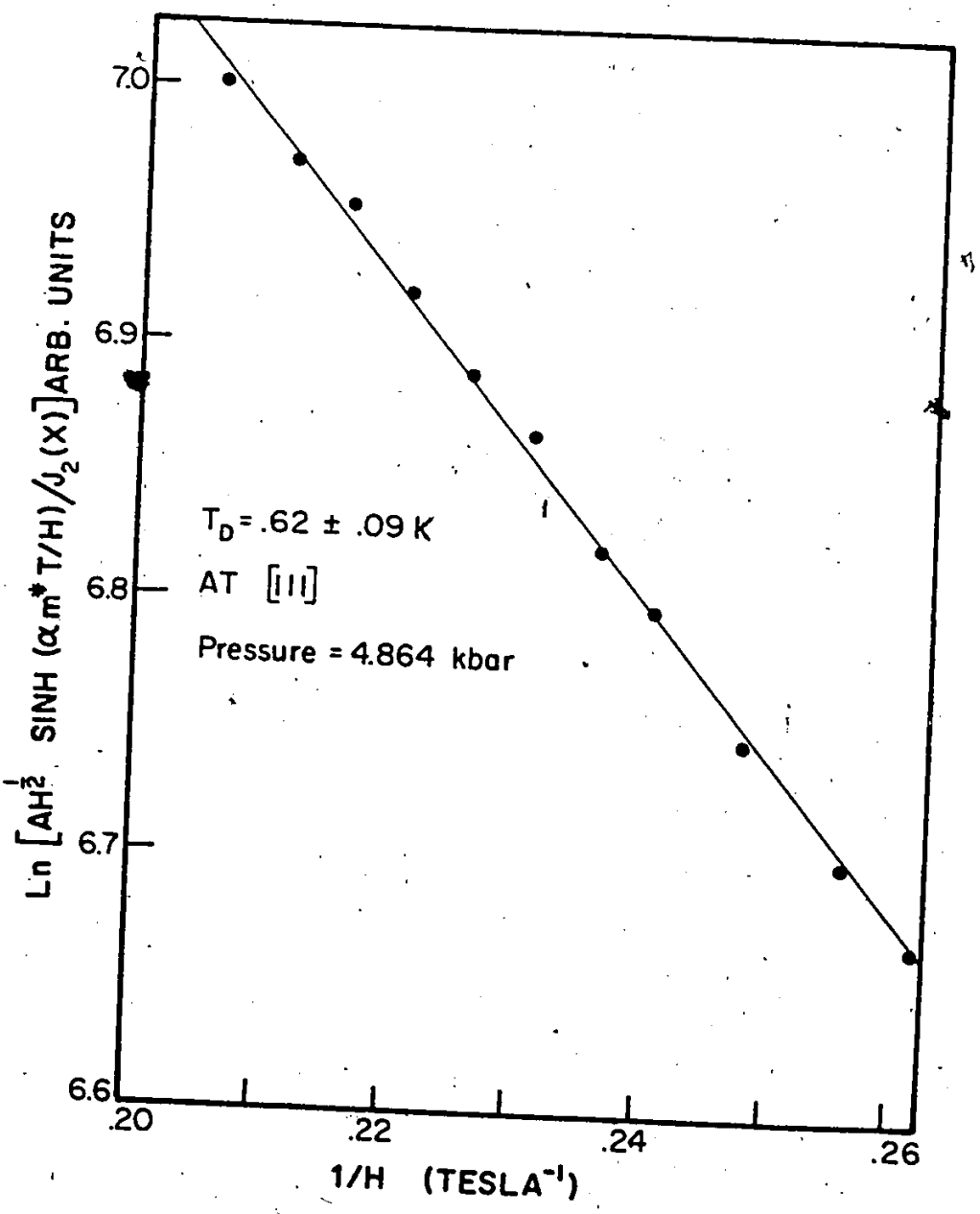

Figure 17

Log plot for the determination of the Dingle temperature T_D of ReO_3 for the α branch along the [111] direction.

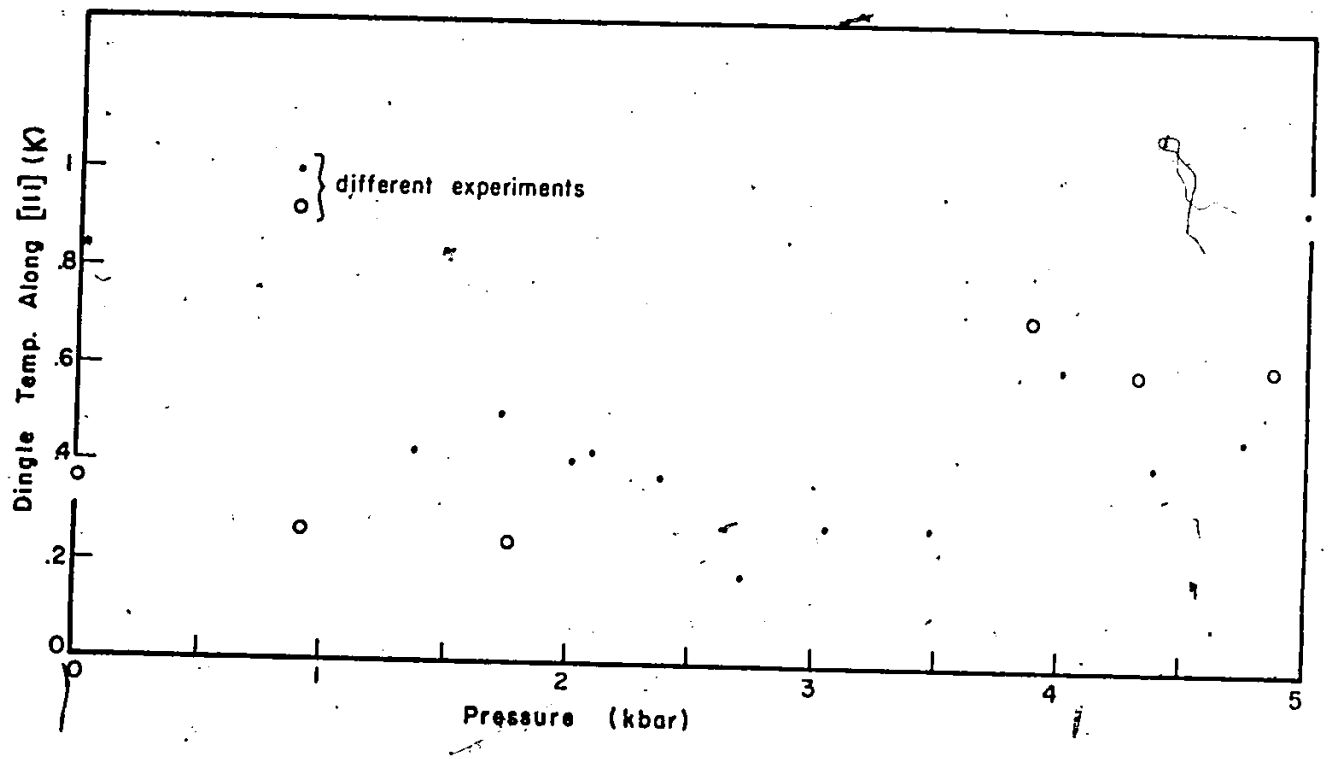

Figure 18

Pressure dependence of the Dingle temperature T_D of ReO_3 for the α branch along the [111] direction.

Table 4. Pressure dependence of dHvA frequencies in ReO_3

Pressure dependence along [111]		Pressure dependence of frequencies along [001]				
Pressure kbar	α(111) Tesla	Pressure	α	γ_1	β	γ_2
0.	4614.1	0.	4153.7	4891.6	6173.2	8817
0.72	4614.95	0.67	4155	4892.6	6174.3	8820
1.32	4615.9	0.86	4155.4	4893.7	6175.2	8822
1.7	4617.2	1.13	4155	4894.2	6175.8	8820
2.07	4616.75	1.40	4155.7	4893.3	6176.9	8818
2.42	4617.4	1.65	4154.6	4894.1	6175.6	8818
2.68	4617.3	1.92	4155.8	4893.4	6176.9	8822
3.	4619	2.25	4156.6	4894.2	6175.8	8822
3.28	4623	2.47	4156.65	4895.1	6176.3	8820
3.45	4625.5	2.66	4157.3	4895.8	6178.1	8823
3.8	4628	2.8	4157.8	4896	6178.8	8825
4.1	4632.9	3.1	4159.5	4897.8	6180.3	8827
4.29	4635.6	3.27	4160.7	4898.4	6183.1	8831
4.48	4637.5	3.54	4162.8	4900	6187.9	8837
4.85	4641	3.75	4164.6	4901.3	6189.3	8845
5.06	4642.5	3.88	4169.5	4904.8	6195.4	8847
		4.14	4170.6	4910.5	6198.4	8850
		4.41	4177.	4916.	6263.	8871
		4.86	4180.	4918.4	6207.8	8876

Table 5. Compressibility of Fermi surface cross-section areas of ReO_3

Frequency and field direction	Area compressibility (10^{-4} kbar^{-1}) 0–25 bar (Schirber et al.1972)	KKR calculation	Present Results low pressure	high pressure
α[111]	4.0±0.3	3.64	3.2±0.4	25±1
α[001]	4.0±0.3	3.74	3.2±0.4	31±2
β[001]	-------	6.42	4.3±0.5	25±3
γ_1[001]	1.5±0.5	0.64	2.1±0.6	27±3
γ_2[001]	-------	3.76	1.4±1.0	34±3

mosaic structure or bending of the sample change the Dingle temperature measured from the dHvA amplitudes (Shoenberg 1962, 1969).

The value for G ($G = \frac{\cos\pi s}{\cos 2\pi s}$) was found from the amplitude ratio of fundamental and second harmonics. As was described in III-c an ambiguity exists since different values of n±s ($s = \frac{1}{2}$ m*g and n is any integer) give the same value of G. The first three possible values of the g-factor are drawn in Table VI. The g-factor for each column in Table VI are the same within experimental error. The average value of the g-factor for the second column is 1.94 with a standard deviation of .065 which might be the proper choice for the g-factor since it is close to the free electron value of 2.0023.

The resistivity of ReO_3 as a function of pressure is shown in Fig. 19 for temperatures of 296 and 110 K. At 296K, the resistivity rises continuously with pressure with a change in slope at 1.2 kbar. At 110 K the resistivity also increases continuously with pressure. However, the change in resistivity is larger: the change at 5 kbar with respect to that at zero pressure is about 60% at 110 K and 10% at room temperature. The normalized slopes of resistivity as a function of pressure are 0.02 and 0.18 $kbar^{-1}$ for room temperature and 110 K, respectively. Below 77 K, the signal was of the order of 10^{-7} volts and the measuring technique was not sensitive enough to detect the change of resistivity with pressure. The value of the resis-

Table 6. Pressure dependence of g-factor in ReO_3

Pressure (kbar)	g-factor ±4%		
5.12	.98	1.9	3.89
4.86	.95	1.93	3.83
4.32	.84	2.04	3.72
4.03	.93	1.91	3.86
3.89	.91	1.97	3.79
3.50	.96	1.93	3.84
3.06	.91	1.97	3.79
3.06	.91	1.97	3.80
2.71	.95	1.93	3.83
2.39	.97	1.91	3.85
2.09	.94	1.94	3.82
2.11	1.02	1.86	3.91
1.73	.91	1.97	3.79
1.38	.91	2.09	3.68
.91	.90	1.98	3.79
0	1.06	1.82	3.97

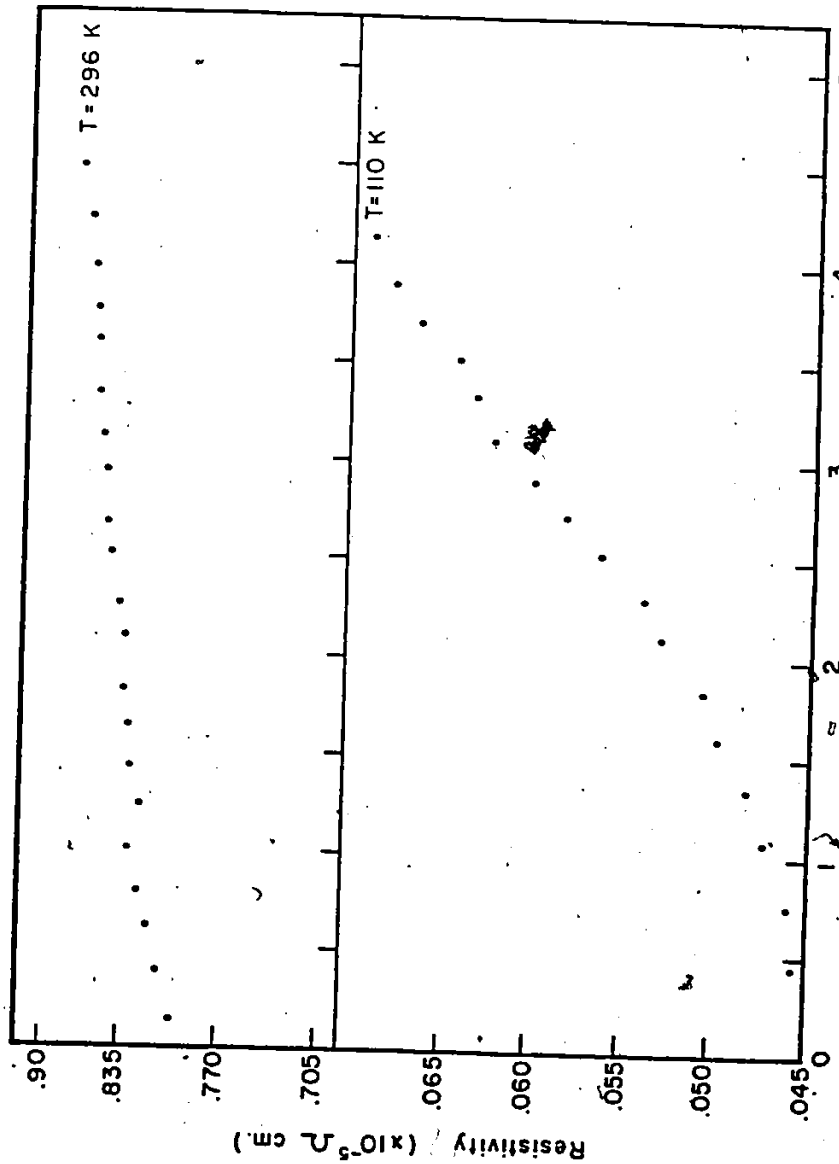

Figure 19

Pressure dependence of resistivity of ReO_3 at 296 K and 110 K.

tivity at 77 K and 4.2 K are $(7.9\pm.3)\times10^{-7}$ and $(5.0\pm5)\times10^{-8}$ Ω-cm, respectively. The resistivity at room temperature (7.89×10^{-6} Ω-cm) was in close agreement with previous results (Ferretti et al. 1965, Pearsall et al., 1974) and the residual resistance ratio was found to be $\frac{\rho_{room}}{\rho} \approx 160$.

b. Discussion

Schirber et al. (1972) measured the isothermal compressibility k_T of ReO_3 at room temperature, as a function of pressure up to 3 kbar using X-ray techniques. The area compressibility of the ReO_3 was determined from the isothermal compressibility k_T using the free electron scaling prediction (eq. II.29).

$$\frac{1}{A}\frac{dA}{dP} = \frac{2}{3} k_T.$$

The free electron scaling prediction of the area compressibility is 3.6×10^{-4} $kbar^{-1}$ and is in agreement within experimental error with the measured values between 0 to 3 kbar for the nearly-spherical α surface but does not agree with that found for the β and γ surfaces. This disagreement may occur since the β surface is less spherical and the γ surface is a multiply-connected surface. The KKR calculations of Myron et al. (1973) of the pressure derivative of the dHvA frequencies of ReO_3 does, in fact, show that the β and γ_1 frequencies do not follow the free electron scaling prediction. However, the calculated pressure derivatives are different from that observed. The

calculated value for the γ_2 orbit is similar to the free electron scaling value which is not found experimentally. The results of the low-pressure area compressibilities are not significantly different from those determined with the fluid helium phase-shift method (Schirber et al., 1972).

In the high pressure region (above 2.4-3 kbar), the area compressibilities are one order of magnitude higher than the initial area compressibilities. This increase in the area compressibilities in the high pressure region cannot be attributed to experimental causes. For example, it is not a result of incorrect pressure reading because a pressure of 19 kbar would be required according to the free electron scaling model to account for the α frequency observed at 5 kbar.

Also it is not due to rotation of the sample when pressure was applied because the pressure dependence was independent of the order of the pressure values at which data were taken and was reproducible in different experiments with different mountings of the sample. Moreover, a sample rotation of 6° would have had to occur to cause the increase in the γ_1 frequency, which has a sec θ dependence where θ is measured from the [001] direction. The increase of dHvA frequency with pressure is similar for all Fermi surface pieces. This can be seen clearly in Fig. 20 where the normalized frequencies are plotted against pressure.

Figure 20

Pressure dependence of the dHvA frequencies normalized to the frequencies at zero pressure for the magnetic field parallel to the [001] directions.

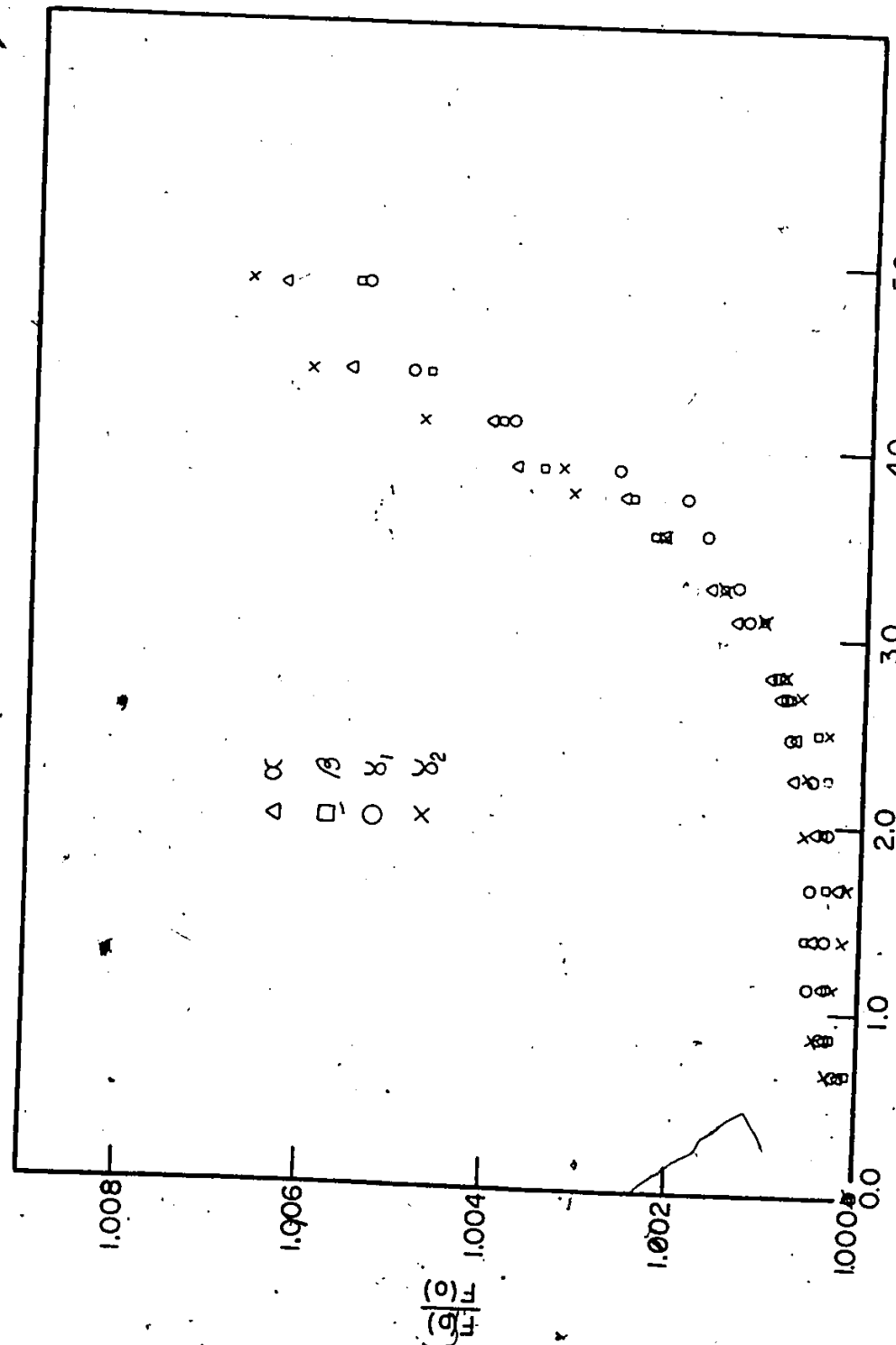
1.008
1.006
1.004
1.002
1.000
0.0
1.0
2.0
3.0
4.0
5.0
PRESSURE (kbar)
$\frac{T(P)}{T(0)}$
α
β
γ_1
γ_2

Two mechanisms may be responsible for the behaviour of the area compressibility of the ReO_3 crystal at high pressures. It has been shown that the bonding in ReO_3 is a mixture of ionic and covalent bonding (Mattheiss, 1969) and the conduction band in ReO_3 arises from the π bonding between rhenium t_{2g} (d band) and the oxygen 2p orbitals . In his APW calculation, Mattheiss (1969) has also shown the effect of oxygen-rhenium hybridization on the ReO_3 conduction bands. Fig. 21(a) shows the APW band calculation involving $V_m(r) + V_\Delta(r)$ (muffin-tin potential plus correction term) along the [100] direction. The results of similar band calculations in which the potential within the oxygen muffin tin spheres was set equal to zero is shown in Fig. 21(b). This assumption for the oxygen potential has produced important changes in the conduction band. The interesting result is that the ordering of the Γ_{12} and $\Gamma_{25'}$ states has been reversed and both the e_g and t_{2g} band widths have been reduced. At high pressures, the overlap between the oxygen and rhenium atoms may increase and enhance the covalent bonding between the oxygen p and the rhenium d orbitals. These changes at high pressures might cause a broadening of the t_{2g} band width and thus a change in the Fermi surface.

Dupree and Holland (1967) obtained an upper limit $\delta_{g_{max}}$ to the spin orbit g-shift from the free electron value g = 2.0023 and is given by

$$|\delta_{g_{max}}| = \frac{4\ell_j \cdot {}^2\Delta_j}{(2\ell_j+1)|\Delta E|}$$

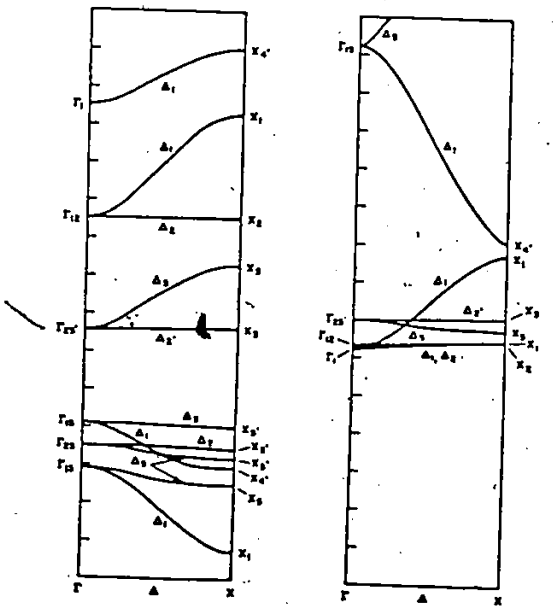

Figure 21

(a) APW results for ReO_3 along the Δ line involving the muffin-tin potential $V_m(r) + V_\Delta(r)$.

(b) APW results involving $V_m(r) + V_\Delta(r)$, in which $V_m(r)$ is set equal to zero within the oxygen spheres.

where Δ_j is the largest atomic-spin-orbit coupling constant for atomic orbitals contributing to the conduction electron wavefunction, ℓ_j is corresponding azimuthal quantum number, and ΔE is the band gap to the nearest state of appropriate symmetry type. The broadening of the t_{2g} band width might also cause a change in energy gap ΔE or in other words, a change in $|\delta g_{max}|$. Unfortunately the values of g factors at different pressures were not accurate enough to reveal such a change. The uncertainty in the g-factor values is about 4% and arises mainly from the uncertainty in effective mass and Dingle temperature. However, the g-factor values show deviations from the free electron value 2.0023 which can provide information about the spin-orbit interaction and many body effect in ReO_3.

There are variations in the Dingle temperature with application of pressure because strain that causes electron scattering is induced during freezing. The amount of strain depends on the rate of freezing and other variables. For example at 1.73 kbar the Dingle temperature for two different experiments are (0.51±.01)K and (0.24±.01)K. This large difference between the Dingle temperatures at the same pressure indicates that the uncertainty due to induced strain in the results of Fig. 18 is high and it gives considerable error in measuring variation of Dingle temperature caused by other means. Within this uncertainty, there appears to be no large change in the Dingle

temperature when the area compressibility is large indicating no large electron scattering.

Another possible explanation is a phase transition involving the displacement of the oxygen atoms from their octahedral sites. This, in fact, has been observed for some perovskite structures such as $SrTiO_3$, where the oxygen atoms undergo a small displacement from their octahedral sites at 110 K (Goodenough et al, 1970). Mattheiss (1972) showed such a displacement has a profound effect on the energy band of $SiTiO_3$. For the ReO_3 compound, Pearsall and Coldren (1976) found a significant difference between the Debye temperature calculated from the resistivity measurement and ultrasonic measurements. They also observed that elastic constants in ReO_3 increase between liquid helium and room temperature in contrast to the normal metal (in normal metal the elastic constant decreases by a factor of 1 to 2% as a result of lattice anharmonicity). Similar results were also reported by Tsuda et al., (1976) measuring the elastic constants by a rectangular parallelepiped resonance technique. Pearsall and Coldren (1976) suggested a possible phase transition at low temperature which involves the displacement of the oxygen atoms from their perfect octahedral sites. Such transition might change Re-O bonding and this may have a similar effect on the energy band and Fermi surface of ReO_3 as was described before.

If the anomaly in ReO_3 at high pressure is due to an electronic or structural transition, it should be observed in the pressure dependence of the resistivity. Resistivity allows one to probe at higher temperatures where the dHvA effect can not be used. There is a change at 1.2 kbar in the slope of the pressure dependence of the resistivity at room temperature. This suggests the possibility of a change at room temperature. However, a structural transition was not detected by Schirber (1972) in an X-ray experiment up to 3 kbar. If it does indicate the transition observed at low temperatures, then the transition pressure does not change significantly with pressure. Changes of resistivity with pressure are much larger at 110 K. The change between 1 and 4 kbar is 54%. This is occurring over the same pressure range as changes in dHvA frequency. Thus it could be due to the same effect. By comparison to the behaviour of the phase transition temperature of the perovskite compounds with pressure, such as $SrTiO_3$, where the 110 K phase transition at zero pressure occurs at 344 kbar at room temperature (Sorge et al., 1970). Thus, if the anomaly observed at low temperatures in ReO_3 corresponds to the displacement of the oxygen atoms, then a much higher pressure is required in order to observe such a transition at room temperature in the resistivity of ReO_3. It was not possible to achieve a higher pressure with the present system and at liquid helium temperature the resistivity of ReO_3 is in order of 10^{-8} Ω-cm

which is very difficult to detect with the four probe technique.

The energy band calculation of Myron et al., (1973) did not show a transition above 3 kbar because the lattice constant was the only parameter that was changed to simulate a high pressure situation. Therefore, an APW energy band calculation is required to determine how the oxygen 2p and rhenium 5d orbitals and their overlap change with pressure. Also, low-temperature, high pressure X-ray studies of ReO_3 are important to study the possible displacement of the oxygen atoms.

CHAPTER VI

CONCLUSION

The topology of the Fermi surface of ReO_3 was studied by means of the induced torque technique. A number of open orbit directions were found from the field dependence of the corresponding induced torque peaks. The stereographic projection of the induced torque peaks indicated that the primary open orbit is along the <100> directions and the higher open orbit directions <110>, <210> ... are also present. The three dimensional grid used by Lifshitz and Peschanskii (1959) to describe a connected topology, supports the open orbits found in the experiment. The connected surface of the APW Fermi surface model adequately explains the open orbit structure. The effective conductivity was found to be constant at different high field values which indicates that the asymptotic behaviour of the effective conductivity is constant in the high field limit. Thus a close agreement with the theoretical calculation is established.

From the pressure dependence of dHvA frequencies, the change in the Fermi surface of ReO_3 with pressure was studied. The dHvA frequencies change linearly with pressure up to 2.4 to 3 kbar and then increase at the faster rate with pressure. The relative change in frequencies between 2.4 and 5 kbar is about

.55% for the α and γ_2 frequencies and .45% for the β and γ_1 frequencies.

From the dHvA results, the area compressibilities for different orbits were calculated. For spherical α Fermi surface sheet the low pressure area compressibility agrees with the free electron model. But, for β and γ Fermi surface sheets the low pressure area compressibilities did not follow the free electron model predictions because the β Fermi surface sheet is less spherical and the γ surface is a multiply connected surface. In the high pressure region above (2.4-3 kbar), the area compressibilities are one order of magnitude larger than the initial area compressibilities.

The pressure dependence of the Dingle temperature and g-factor were deduced from the amplitude and phase of the dHvA frequency of the α Fermi surface sheet. It was found that the Dingle temperature is sensitive to the duration of the applied pressure on the sample and also to the cooling rates of the sample for obtaining the desired hydrostatic pressure. The g-factor at different pressures shows a deviation from the free electron value 2.0023 but the uncertainty in the results was large (relative error 4%) and it was not possible to observe appreciable changes in the spin-orbit interaction induced by pressure.

The resistivity of ReO_3 as a function of pressure up to 5 kbar was measured at different temperature (296 and 110 K).

The resistivity increases continuously with pressure for both temperatures except, for a change in the slope at 1.2 kbar at room temperature.

At 110 K, the resistivity changes at a faster rate with pressure compared to the rate of changes of resistivity at room temperature. This might be an indication of the anomaly observed in dHvA experiments. But, the present resistivity data are not sufficient enough to confirm this, therefore, measurements of resistivity at higher pressure than 5 kbar and different temperatures are needed.

Possible explanations for this behaviour of the area compressibilities of ReO_3 crystals at high pressure were suggested. At high pressure the covalency between the oxygen 2p and rhenium 5d orbitals may increase and cause a change in the Fermi surface of ReO_3. Another possible explanation is a phase transition involving the displacement of the oxygen atoms from their octahedral sites. Low temperature, high pressure X-ray studies as well as an APW energy band calculation as a function of pressure are required in order to find the complete cause of the high pressure anomaly in the dHvA results of ReO_3.

SECTION 2

STUDY OF FERMI SURFACE OF $Hg_{2.86}AsF_6$

CHAPTER VII

Introduction

Recently there has been considerable interest in the quasi-one-dimensional mercury chain compound $Hg_{2.86}AsF_6$ (hereafter $Hg_{3-\delta}AsF_6$). This compound was first grown by Cutforth et al. (1975). The X-ray studies of Brown et al. (1974) reveal that this compound crystallizes in a body-centred tetragonal lattice with four formula weights of $Hg_{3-\delta}AsF_6$ per unit cell. The array of well separated AsF_6 octahedra form extremely narrow non-intersecting channels ($\sim$ .3 Å in diameter) along the a and b directions of the tetragonal cell. Chains of mercury ions run along these channels. The intrachain Hg-Hg distance a_{Hg} is incommensurate with the tetragonal lattice constant a_L yielding to $\frac{a_L}{a_{Hg}} = 3-\delta = 2.86$ at room temperature (Brown et al., 1974) and $\frac{a_L}{a_{HG}} = 3-\delta = 2.79$ (Hastings et al., 1977) at 10 K. At room temperature, the mercury chains can be considered as a one-dimensional liquid and mercury ions can move along the chains. However, as the temperature is lowered at 180 K, interchain coupling between parallel chains forms short range order (Hasting et al.,1977) and below 120 K coupling between perpendicular chains cause long range order between mercury ions (Pouget et al., 1978).

This compound is metallic and remains metallic down to 1 K with an anisotropic behaviour in the electrical conductivity (Cutforth et al., 1977; Chiang et al., 1977). The conductivity along the a and b directions is about 200 times higher than that along the c direction. This behaviour is also observed in the optical measurements of Batalla (1976) and Peebles et al., (1977). Over the last three years, extensive work has been done on this compound in terms of thermoelectric power (Scholz et al., 1977), magnetic susceptibility (Wei et al., 1977), nuclear magnetic resonance relaxation time (Ehrenfreund et al., 1977) and the differential thermal analysis (Datars et al., 1978). The ultimate goal of these experiments was to provide information in order to understand the behaviour of electrons in this and the related compound $Hg_{2.91}SbF_6$.

In this study, information about the Fermi surface of $Hg_{3-\delta}AsF_6$ compound will be given using the dHvA technique as a tool hoping the Fermi surface results to be useful for obtaining the band structure for this quasi one-dimensional compound.

In chapters VIII and IX, a brief discussion about the structure of $Hg_{3-\delta}AsF_6$ and experimental technique will be given. In chapter X the results and discussion will be presented.

CHAPTER VIII

$Hg_{3-\delta}AsF_6$ CRYSTAL STRUCTURE

$Hg_{3-\delta}AsF_6$ crystallizes in a body centred tetragonal space group $I4_1/amd$ with four formula weights of $Hg_{3-\delta}AsF_6$ per unit cell. This compound contains infinite non-intersecting chains of mercury ions running along [100] and [010] directions of the tetragonal structure formed by the $[AsF_6]^{-1}$ octahedra. Fig. 22 shows the unit cell of this compound with two channels of mercury ions running along the [100] direction with positions at (0,0) and $(\frac{1}{2},\frac{1}{2})$ in the (100) plane and two other channels of mercury ions running along the [010] direction with positions at $(\frac{1}{4},\frac{1}{4})$ and $(\frac{3}{4},\frac{3}{4})$ in the (010) plane. The separation between mercury ions 2.67 Å, is incommensurate with the tetragonal lattice parameter a_L = 7.53 Å (Brown et al., 1974; Hastings et al., 1977). It should be noted here that the separation between mercury ions in metallic mercury is about 3.005 Å (Barrett, 1957) which is greater than the Hg-Hg distance and slightly less than the interchain distance along the c-axis.

At room temperature, no order exists between the positions of the mercury ions in the adjacent chains. However, at 180 K, a short range order exists because of the coupling between

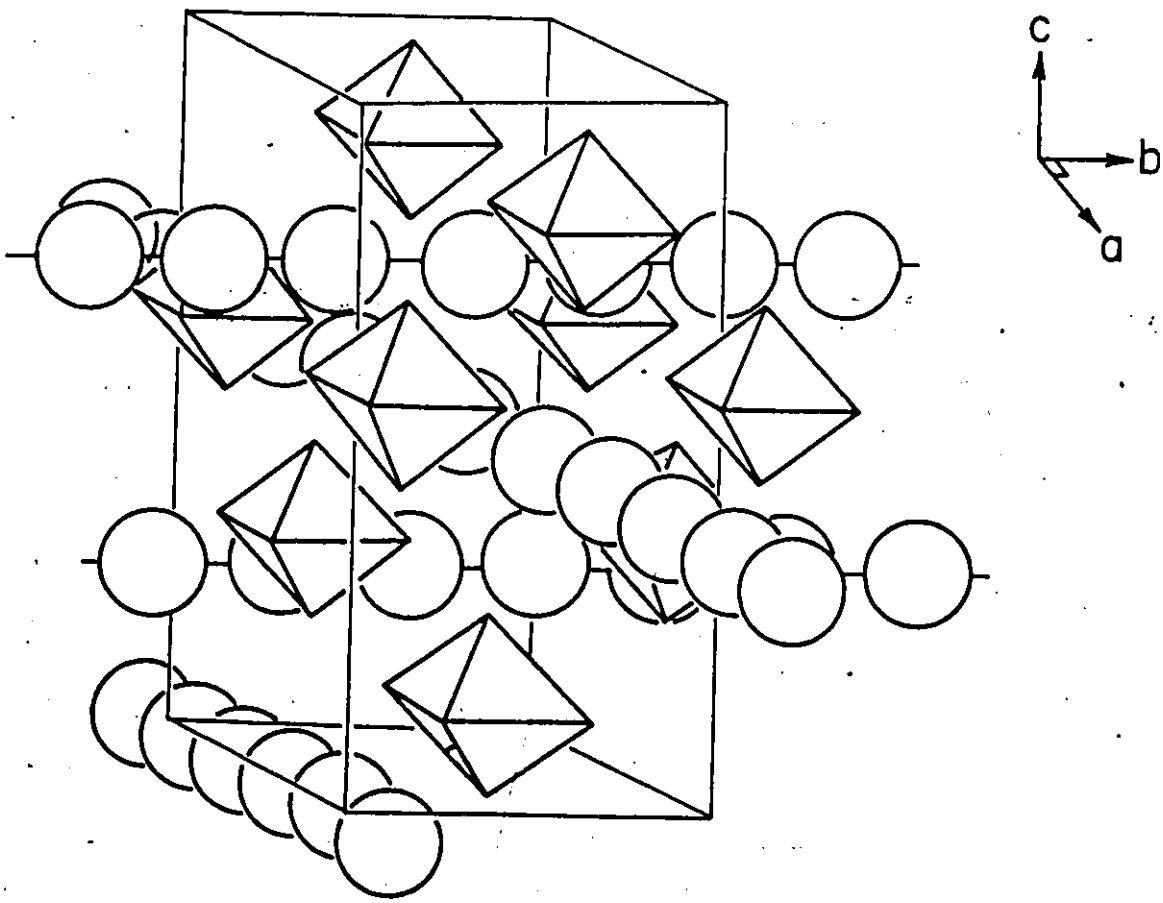

Figure 22

Isometric view of $Hg_{3-\delta}AsF_6$ showing the chains of mercury atoms (circles) in the $(AsF_6)^-$ (octahedral) lattice.

parallel chains; below 120 K, coupling between perpendicular chains causes long range order between the mercury ions (Hastings et al., 1977; Pouget et al., 1978). The crystal data is summarized in Table 7 (Brown et al., 1974; Hastings et al., 1977).

Table 7 Crystal data for $Hg_{3-\delta}AsF_6$

System	tetragonal
Space group	$I4_1/amd$
Lattice parameter	
a_L	7.54 Å at 300 K 7.442 Å at 10 K
c_L	12.395 Å at 300 K 12.248 Å at 10 K
Interchain mercury distance	2.67 Å
Interchain distance	
$\hat{a}$ and $\hat{b}$	7.54 Å at 300 K 7.442 Å at 10 K
$\hat{c}$	3.08 Å at 300 K 3.062 Å at 10 K
$\delta = (3a_{Hg}-a_L)/a_{HG}$	0.18 Å at 300 K 0.21 Å at 10 K
Cell volume (room temperature)	701.1 $Å^3$
Formula weight	573.7 gr.
Number of formula units per unit cell	4

CHAPTER IX

EXPERIMENTAL TECHNIQUE

The $Hg_{3-\delta}AsF_6$ compound was kindly prepared by D. Chartier of the Chemistry Department, McMaster University. The samples were prepared by direct contact of a mercury surface with a solution of arsenic pentafluoride (AsF_5) in liquid SO_2 at -10 degree centigrade (Chartier et al., 1978). The single crystals used in this study were about $2\times2\times1$ mm^3.

The $Hg_{3-\delta}AsF_6$ compound is extremely hygroscopic. A special sample holder was designed in order to prevent any contact of the sample with air. The sample holder was made of Kel F and was cylindrical with a 2 cm height and 3 cm diameter. The procedure of mounting the sample took place inside a dry box.

The low frequency modulation technique was used to detect dHvA oscillations. This technique is described in section 1, chapter III-c. The dHvA frequencies were detected at the second harmonic of 517 Hz. To study the low and high frequency ranges, different modulation fields were chosen to optimize conditions for the Bessel function term in the dHvA amplitudes. The detailed electronic processing and the

pick-up coil assembly has been described by Dunsworth (1972).

A 5.5 tesla Westinghouse superconducting solenoid was used to provide the d.c. magnetic field. A field range of 2.6-5.5 tesla was used to observe the dHvA oscillations in $Hg_{3-\delta}AsF_6$. Data were collected on magnetic tape and Fourier analyzed by computer. The dHvA frequencies and amplitudes were found from the Fourier transform spectrum. All the frequency data were taken at 1.1 K. For the mass measurements, the temperatures were obtained from the liquid helium vapour pressure with a Texas Instrument precision pressure gauge.

The measurements were made for magnetic field directions between the c-axis and the (001) plane which were determined optically. Directions in the isotropic (001) plane could not be determined optically so that it was not known where the plane that was studied intersected the (001) plane. The a-b plane was studied by rotating the crystal about the c-axis.

CHAPTER X

RESULTS AND DISCUSSIONS

a - Results

The dHvA frequencies of $Hg_{3-\delta}AsF_6$ are shown in Fig. 23 as a function of the angle θ between the c-axis and the magnetic field direction. The results consist of low frequency branches α,β, γ and high frequency branches δ, ε and μ. Branches α and γ disappear about $\theta = 71°$ and β disappears at $\theta = 60°$. The amplitudes of the β and γ frequencies are strong in all magnetic field directions while the amplitude of the α frequency is weak in all magnetic field directions, especially near the c-axis. The δ and ε in the high frequency branches disappear about $\theta = 60°$ and the amplitude of δ is dominant in this frequency range. Branch μ disappears about 20° from the c-axis and is not observed below a magnetic field of 4.6 T. In all magnetic field directions, harmonics and combinations of the frequencies were present but are not shown in Fig. 23. It should also be noted that two frequencies with values of 48 T and 235 T were observed in the low frequency range but are not plotted in the figure because they were very weak and appear over a small angular range about the c-axis. Table

Figure 23

de Haas-van Alphen frequencies in $Hg_{3-\delta}AsF_6$ angle θ between the magnetic field direction and the c-axis, in degrees. Solid lines are proportional to $\sec\theta$ as described in the text.

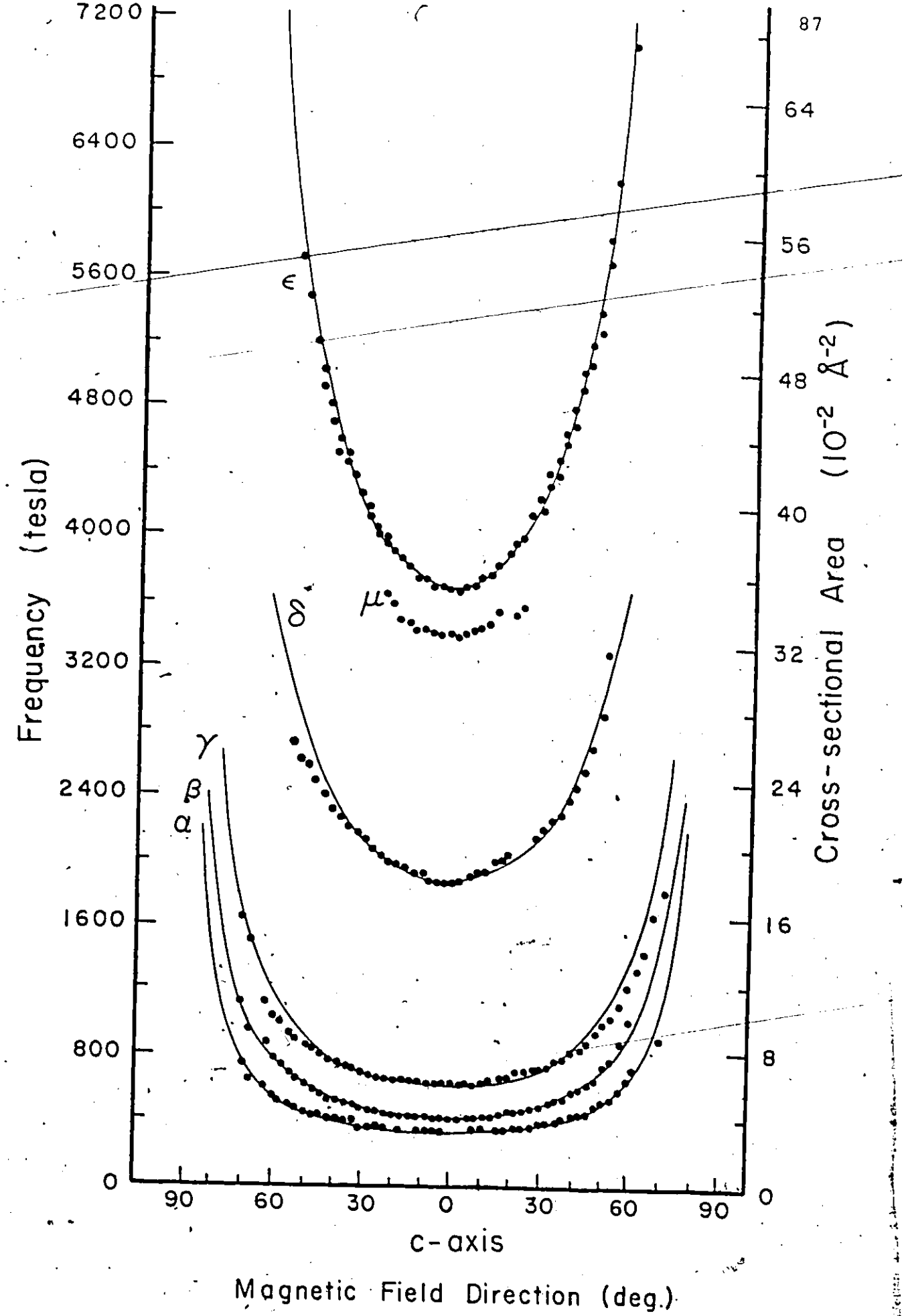
7200
6400
5600
4800
4000
3200
2400
1600
800
0
Frequency (tesla)
87
64
56
48
40
32
24
16
8
0
Cross-sectional Area (10^{-2} Å^{-2})
ε
δ
μ
γ
β
α
90
60
30
0
30
60
90
c-axis
Magnetic Field Direction (deg.)

9 shows the values of the dHvA frequencies and corresponding cross-sectional areas of the Fermi surface measured with the magnetic field along the c-axis.

No closed Fermi surface pieces appear to exist since no dHvA frequencies are found in a careful search with magnetic field directions in the (001) plane.

In an elastic neutron scattering experiment, Pouget et al., (1978) found that high temperature short range order can be frozen in by rapid cooling of $Hg_{3-\delta}AsF_6$ with no evidence of long range order. This evoked two dHvA experiments which were done with one sample at a magnetic field direction 20 degrees from the c-axis. First, the sample was immersed in liquid helium from room temperature and in the second experiment the same sample was warmed up to room temperature slowly and then lowered to liquid helium temperature very slowly. In both cases, the data were taken under the same conditions of magnetic field modulation and magnetic field range. The amplitudes of α, β, γ and ε frequencies increased by a factor of 2 in the second experiment with no change in these frequencies from the first experiment. However, two frequencies appeared at 1919 and 2010 T in both experiments, where the one at 2010 T corresponded to the δ frequency. The amplitude of the 1919 T frequency was nine times larger than the δ frequency for fast cooling of the sample but the reverse is true for slow cooling.

Another difference between the two experiments was the appearance of harmonics and combinations of all dHvA frequencies after the experiment when the sample was cooled slowly.

With the slowly cooled sample, the cyclotron masses were determined from the temperature dependence of the dHvA amplitude. The cyclotron masses of the branches with sufficient amplitude for the mass determination were found to be 0.41, 0.37 and 0.38 m_0 for γ, δ and ε, respectively with an error of ±10%.

The Dingle temperature was also calculated using the field dependence of the amplitude of the γ frequency. The Dingle plot is shown in Fig. 24. In the Dingle plot the amplitudes of the γ frequency shows an oscillatory behaviour which is periodic with inverse magnetic field. The reason for this oscillatory behaviour is that the amplitude modulation (AM) can arise in conjunction with frequency modulation (FM) due to magnetic interaction, through modulation of the Bessel function arguments which appear in using the field modulation technique (Alles and Lowndes, 1973). In this AM-FM effect, the low frequency modulates the amplitude of the high frequency dHvA wave form which causes the oscillatory behaviour of the amplitude of the high frequency. The observed frequency was 57.7 T. The Dingle temperature was determined from the least squares fit of the slope of the Dingle plot and was found to be T_D = 1.2±0.1 K.

Figure 24

Log plot used to determine the Dingle temperature T_D for the γ branch where the magnetic field direction is 20° away from the c-axis. The oscillatory behaviour of amplitude is due to the AM-FM effect with the frequency 57.7 T.

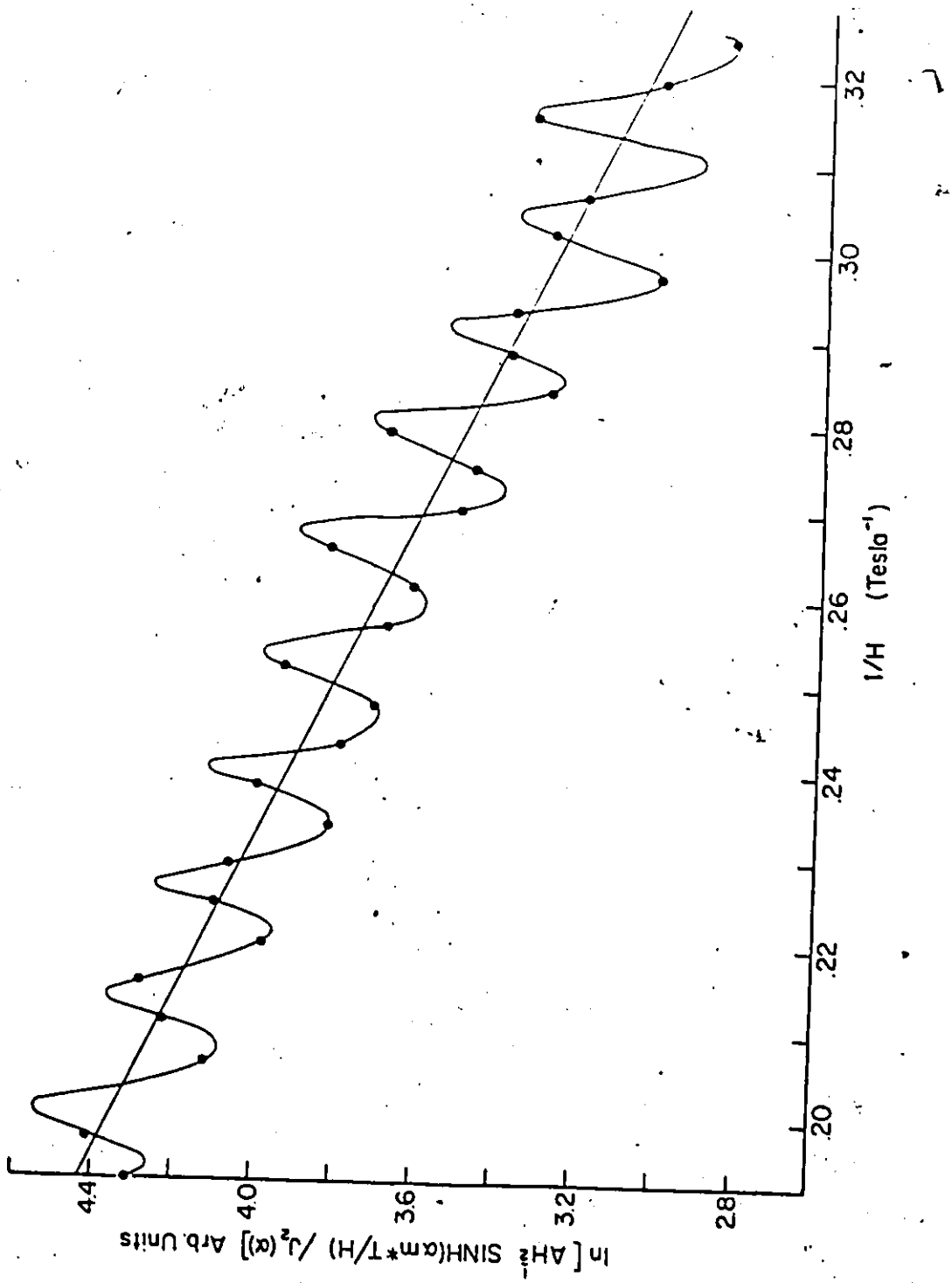
ln [AH^½ SINH(αm*T/H) /J2(α)] Arb. Units
4.4
4.0
3.6
3.2
2.8
.20
.22
.24
.26
.28
.30
.32
1/H (Tesla⁻¹)

b - Discussion

The angular dependence of the dHvA frequencies suggests pieces of Fermi surface which are cylinders along the c-axis in k space. The cross sectional area of a simple cylinder varies as $A_0 \sec\theta$, where A_0 is the cross-sectional area perpendicular to the axis of the cylinder and θ is the angle between the magnetic field direction and the cylinder axis. This can be seen from Fig. 25 where for any angle θ the cross-sectional area of a square cylinder is rectangular with an area of

$$A = a^* \cdot b^* = k_F \cdot k_F/\cos\theta = k_F \cdot k_F/\cos\theta \mp A_0/\cos\theta.$$

The dHvA frequencies in Fig. 23 follow this $\sec\theta$ dependence closely for values of A_0 and corresponding frequencies F_0 given in Table 9. This $\sec\theta$ behaviour is independent of the shape of the area A_0, so that no information about the shape of the cross-section A_0 is obtained from the dHvA effect for a perfectly straight-sided cylinder.

The cylindrical nature of the Fermi surface explains the two-dimensional electrical properties of $Hg_{3-\delta}AsF_6$. Electron velocity, being perpendicular to the Fermi surface, is in the (001) plane for straight sided cylinders. A small conductivity along the c-axis is explained by some of the cylinders having small deviations from a straight cylinder giving an electron velocity component along the c-axis.

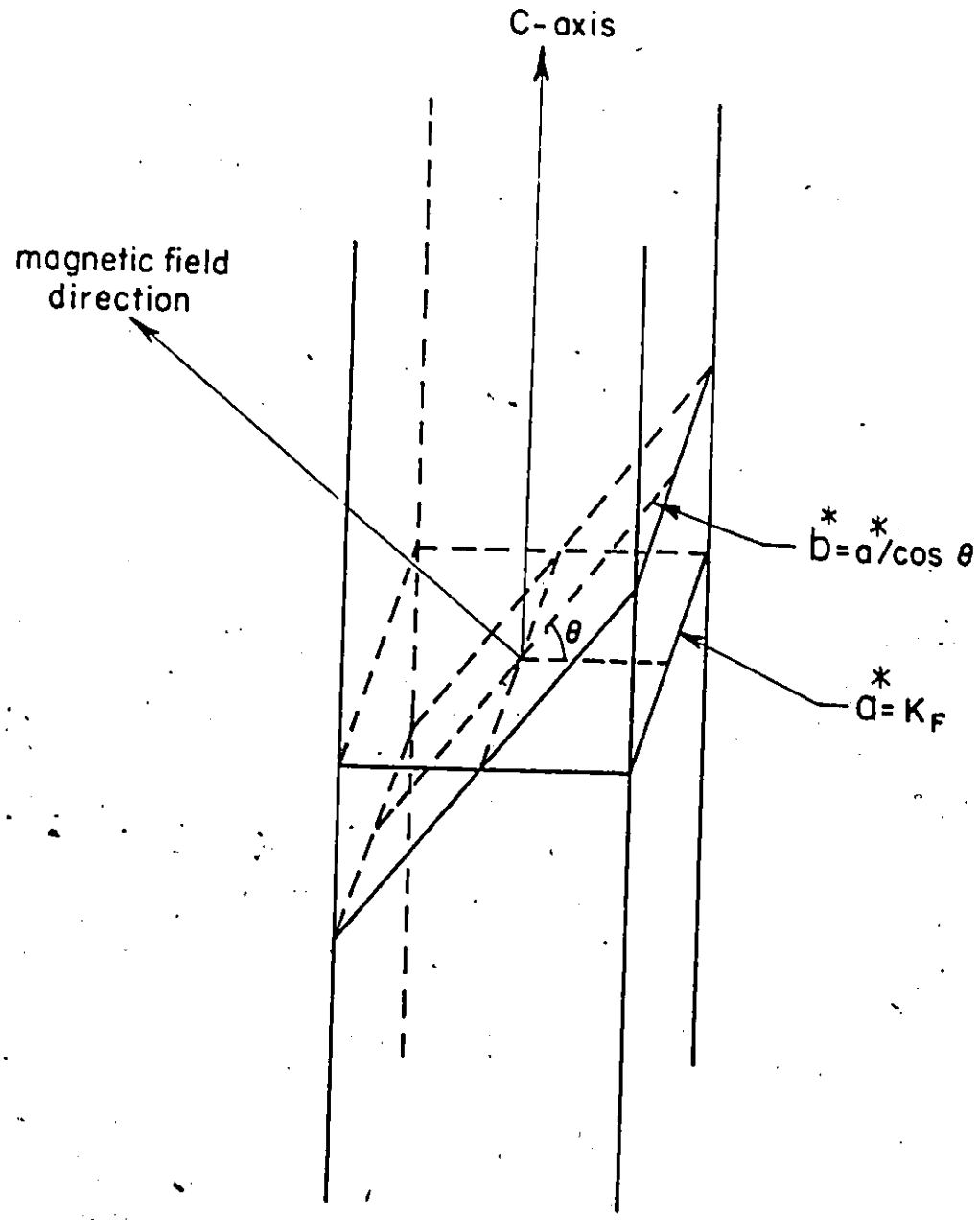

Figure 25

Variation of the cross-sectional area of a square cylindrical Fermi surface. θ is the angle between the magnetic field direction and the c-axis. The magnetic field is rotated along the a-axis.

The origin of the multitude of Fermi surface cylinders that are straight or nearly straight is an interesting question. A calculation using a linear combination of atomic orbitals of the mercury ions predicts a single undulating cylinder as well as a closed surface (Batalla, 1978). Berlinsky (1978) used a simple model for calculating the band structure and obtaining the Fermi surface of this compound. In his calculation the electronic wave function was free electron like along the chains and Gaussian perpendicular to the chains. The wave functions were defined by

$$\psi_{M,k_a} = (a\,N_a)^{-1/2}\, e^{i(k_a + 2M\frac{\pi}{a})x}\, f(y,z) \qquad (X\text{-}1)$$

where a is the lattice constant of the crystal in the a or b directions, aN_a is the crystal thickness along the a direction, k_a is the wave vector of the electron along the a direction $(-\frac{\pi}{a} \leq k_a \leq \frac{\pi}{a})$, M is an integer 0, ±1, and

$$f(y,z) = (\pi\rho^2)^{-1/2}\, e^{-(y^2+z^2)/2\rho^2} \qquad (X\text{-}2)$$

ρ is a parameter and is set to be 1.32 Å. Similar functions ψ_{N,k_b} are formed for the b direction. These functions are localized in the channels where mercury chains exist and the Bloch functions for the crystal (of mercury chains) are defined by

$$\psi_a(\alpha,M,k_a) = (N_a N_c)^{-1/2} \sum_{m,n} \psi_{M,k_a} e^{-ik\cdot\vec{R}_a^{\alpha mn}}$$

and (X-3)

$$\psi_b(\alpha,N,k_b) = (N_b N_c)^{-1/2} \sum_{m'n'} \psi_{N,k_b} e^{ik\cdot R_b^{\beta m'n'}}$$

where $\vec{R}_a^{\alpha mn}$ and $R_b^{\beta m'n'}$ are the positions of the mercury channels and are given by

$$\vec{R}_a^{\alpha mn} = (0,am,cn) + \vec{\sigma}_\alpha$$

(X-4)

$$\vec{R}_b^{\beta m'n'} = (am',0,cn') + \zeta_\beta$$

where $\vec{\sigma}_\alpha$ and $\vec{\zeta}_\beta$ are sublattice vectors and $\alpha,\beta = 1,2$ are sublattice indices which indicate that four mercury chains pass through each unit cell, two each in the a and b directions.

From equations X-3, 12 basis functions for each value of $\vec{k}$ in the first Brillouin zone can be found (M and N are restricted to 0 or ±1, i.e. in the first Brillouin zone). From these wave functions the approximate Hamiltonian was constructed where the diagonal elements are free electron like and are given by

$$\varepsilon_a(\alpha,M,k) = (\frac{\hbar\pi}{a})^2/2m^*(\frac{ak_a}{\pi} + 2M)^2$$

(X-5)

$$\varepsilon_b(\alpha,N,k) = (\frac{\hbar\pi}{a})^2/2m^*(\frac{ak_b}{\pi} + 2M)^2$$

and the off diagonal terms of M are

$$(\psi_a(\alpha,M,\vec{k}),H\psi_b(\beta,N,\vec{k}) = \Delta S_{\alpha\beta}^{MN}(k) \qquad \text{(X-6)}$$

here $S^{MN}_{\alpha\beta}(k)$ is the overlap of two wave functions and Δ is the only adjustable parameter in Berlinsky's model. In the off-diagonal terms in H, only overlaps between the nearest perpendicular chains, were considered.

In this model, if the overlap between the perpendicular chains are said to be zero ($\Delta=0$) the Fermi surface sheets can be constructed by filling the energy levels of eq. (X-5). For each value of M and k, there are 8 states (including spin). The total number of electrons per unit cell are:

2(6S electrons/Hg) × 2.79 (Hg in each chain in a unit cell) × 4 (chains/unit cell) = 22.32 electrons.

Four of these electrons go to AsF_6 molecules. The remaining 18.32 occupy 9.16 states/spin. Thus, the a and b states can be filled up to $(ak_a/\pi + 2M) = \pm 2.29$ for $\alpha = 1,2$ and $(ak_b/\pi + 2N) = \pm 2.29$ for $\beta = 1,2$ respectively. The Fermi energy is $(2.29)^2 \times (\frac{\hbar\pi}{a})^2/2m^* = 3.56$ eV (for $m^* \sim m_0$) and the Fermi surfaces are sheets defined by $k_a = \pm .29\ \pi/a$ and $k_b = \pm .29\ \pi/a$. The energy bands for the case of $\Delta=0$ are shown in Fig. 26. Each energy band is at least two-fold degenerated because of the two parallel chains in $\vec{a}$ or $\vec{b}$ directions. Projection of Fermi surface sheets on the (001) plane is shown in Fig. 27.

Two straight cylinders are formed with even a small overlap of ψ_a and ψ_b. An electron-like cylinder occurs where the Fermi surface sheets along $\vec{a}$ and $\vec{b}$ cross. A hole-like

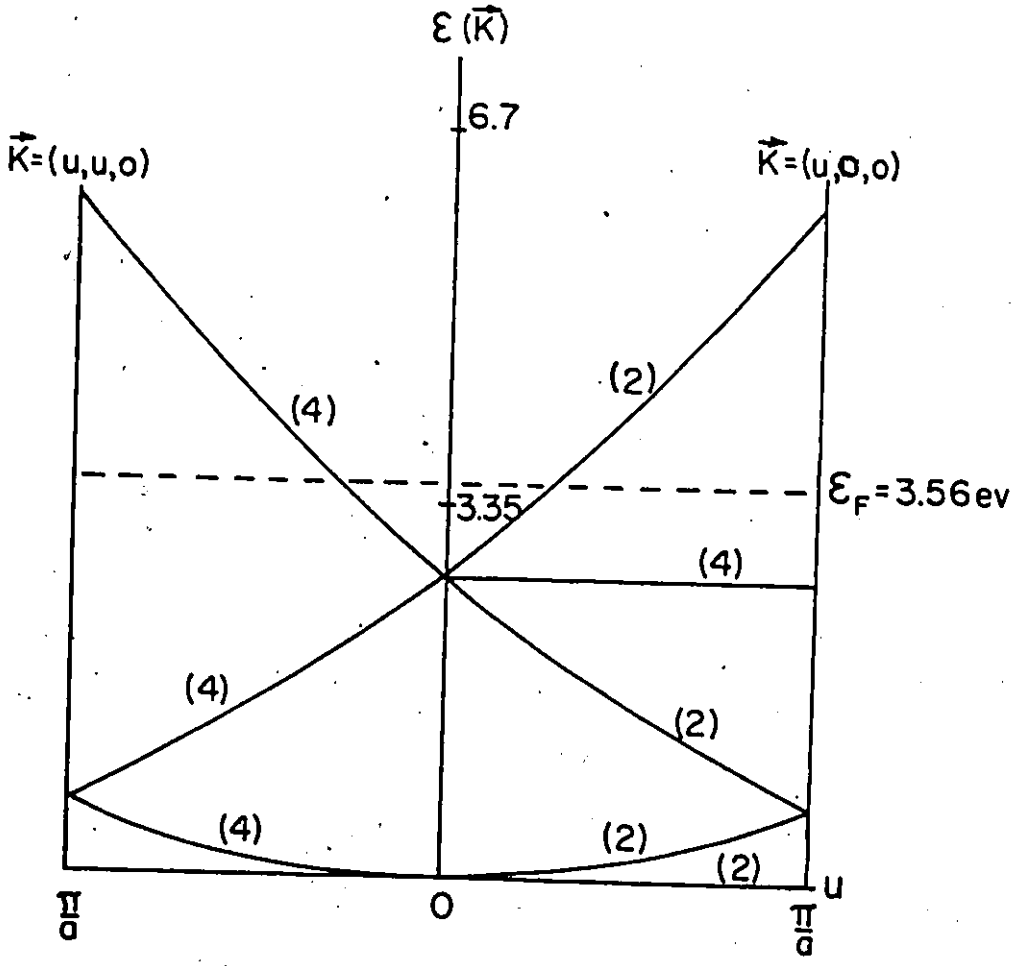

Figure 26

The energy band of $Hg_{3-\delta}AsF_6$ for the case of no interaction ($\Delta=0$) between perpendicular chains. Number in parentheses shows the degeneracy of bands.

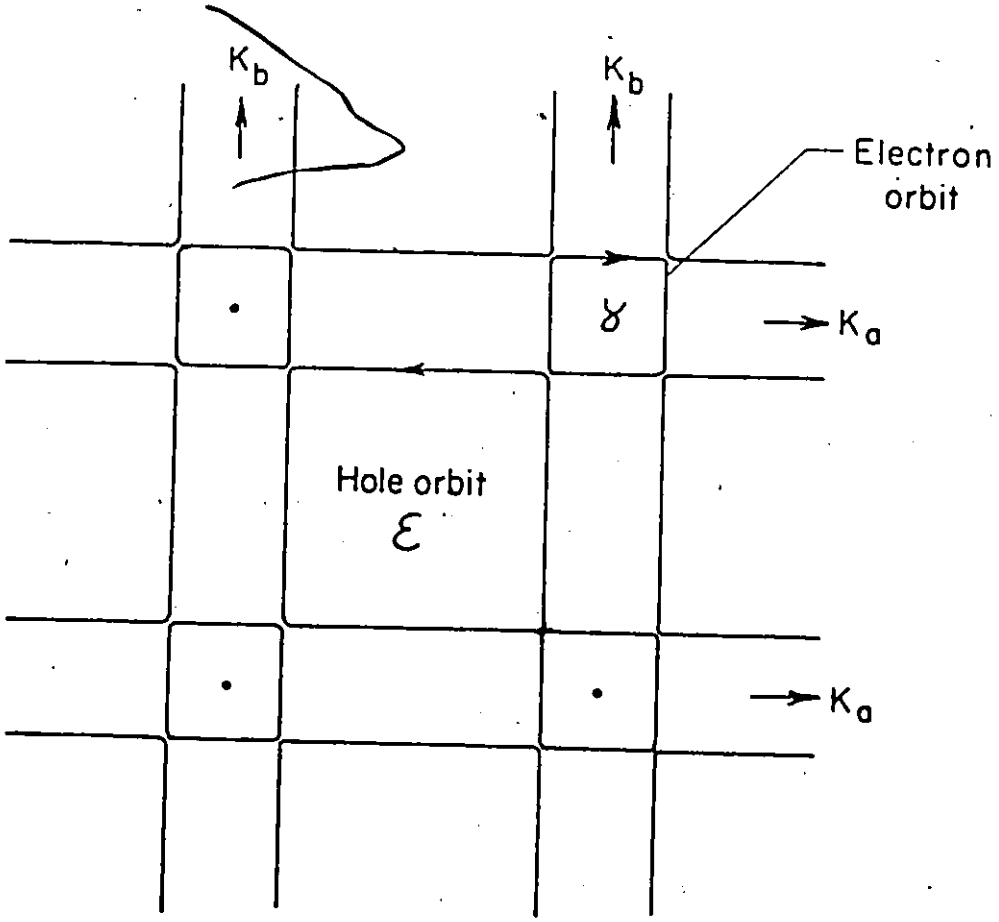

Figure 27

The projection of the Fermi surface cross sectional areas on the ab plane for $\Delta=0$. γ is an electron orbit and ϵ is a hole orbit.

cylinder exists between the sheets. The calculated cross sectional areas and the corresponding dHvA frequencies of these cylinders are given in Table 8 for a magnetic field along the c-axis. The experimental results for the γ and ε branches are also given in Table 8.

Table 8. Theoretical and experimental results of Fermi surface cross sectional area and dHvA frequencies of γ and ε.

	Calculated result		Experimental result	
	Area ($\mathring{A}^{-2}$)	Freq. (T)	Area ($\mathring{A}^{-2}$)	Freq. (T)
γ	5.99×10^{-2}	627	5.98×10^{-2}	626
ε	3.59×10^{-1}	3762	3.52×10^{-1}	3680

The effect of non-zero value of Δ is to remove all of the degeneracies which are not required by the symmetry of the lattice. For large coupling between the perpendicular chains, the theory predicts four undulating cylinders. Six external orbits exist for magnetic fields along the c-axis, because pieces of cylinders have the same cross sectional area at $k_c = \pm \frac{\pi}{c}$. For Δ = 7 the projection of the Fermi surface cross sectional area with corresponding dHvA frequencies is shown in Fig. 28. The agreement between the experimental results and

Figure 28

The projection surface on the ab plane for $\Delta=7$ (one quadrant of Brillouin zone are shown). The number represents the corresponding dHvA frequencies in tesla. The upper, lower figures show the projection of the Fermi surface sheet for $K_c = 0$ and $K_c = \pm\pi/c$, respectively. A, B and C are electron-like orbits and D, E and F are hole-like orbits.

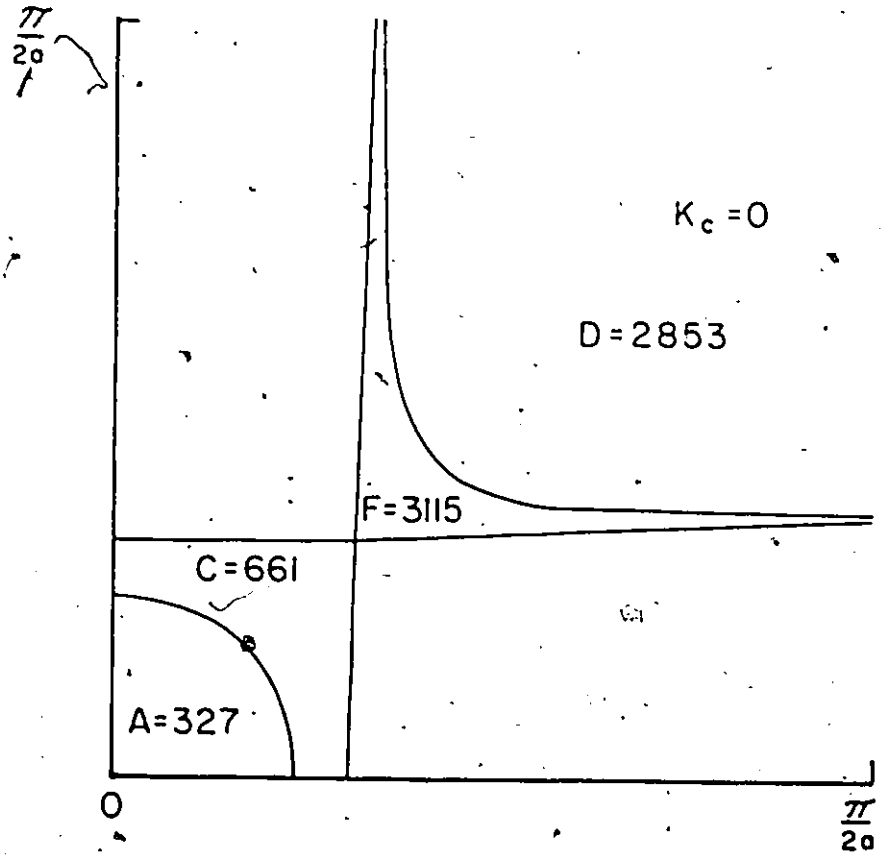
π/2a
$K_c = 0$
D = 2853
F = 3115
C = 661
A = 327
0
π/2a

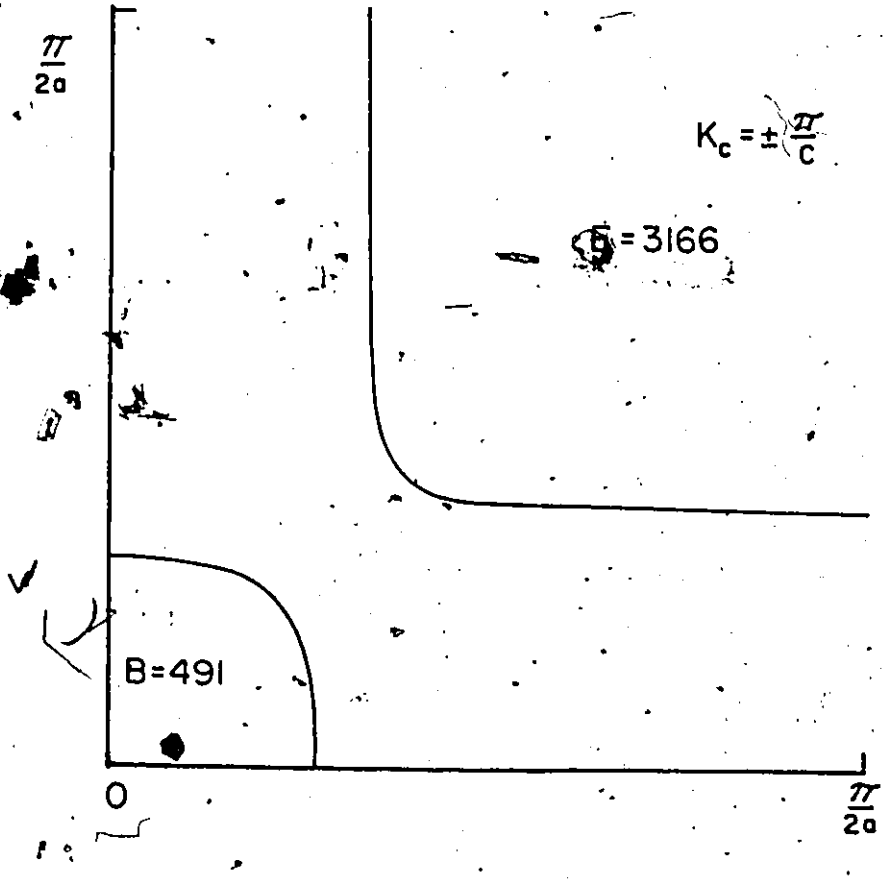
π/2a
$K_c = \pm(\pi/C)$
E = 3166
B = 491
0
π/2a

theory is good for the magnetic field along the c-axis. However, for the magnetic field away from the c-axis B and E branches of Fig. 28 will have two values. Thus, one is expected to see branches of dHvA frequencies which cross each other along the c-axis. The angular dependence of calculated dHvA frequencies for A,B and C are shown in Fig. 29 where it shows that for magnetic fields away from the c-axis two values for B are obtained. The angular dependence of B and F branches was not observed experimentally.

In $Hg_{3-\delta}AsF_6$, the Hg-Hg distances are incommensurate with the tetragonal lattice vector a_L. In the reciprocal space, the difference between the interchain reciprocal lattice vector and the vector spanning three unit cells of the reciprocal tetragonal lattice vector at 10 K is

$$\delta^* = 3 \times \frac{2\pi}{a_L} - \frac{2\pi}{a_{Hg}} = 3 \times \frac{2\pi}{7.442} - \frac{2}{2.67} = .179 \text{ Å}^{-1} .$$

The effects of a super lattice in metal Cr (Graebner and Marcus, 1968; Falicov and Zuckerman, 1967) and compound 2H-$TaSe_2$, (Graebner, 1977; Wilson, 1977) have been shown previously. The superlattice produces an additional periodic structure in addition to the crystal lattice and has a truncating effect on the Fermi surface analogous to the introduction of Brillouin zone boundaries by the ordinary lattice. Thus, under these circumstances the Fermi surface is separated into pieces by energy gaps.

Figure 29

Angular dependence of calculated dHvA frequencies for A, B and C orbits in the ac plane.

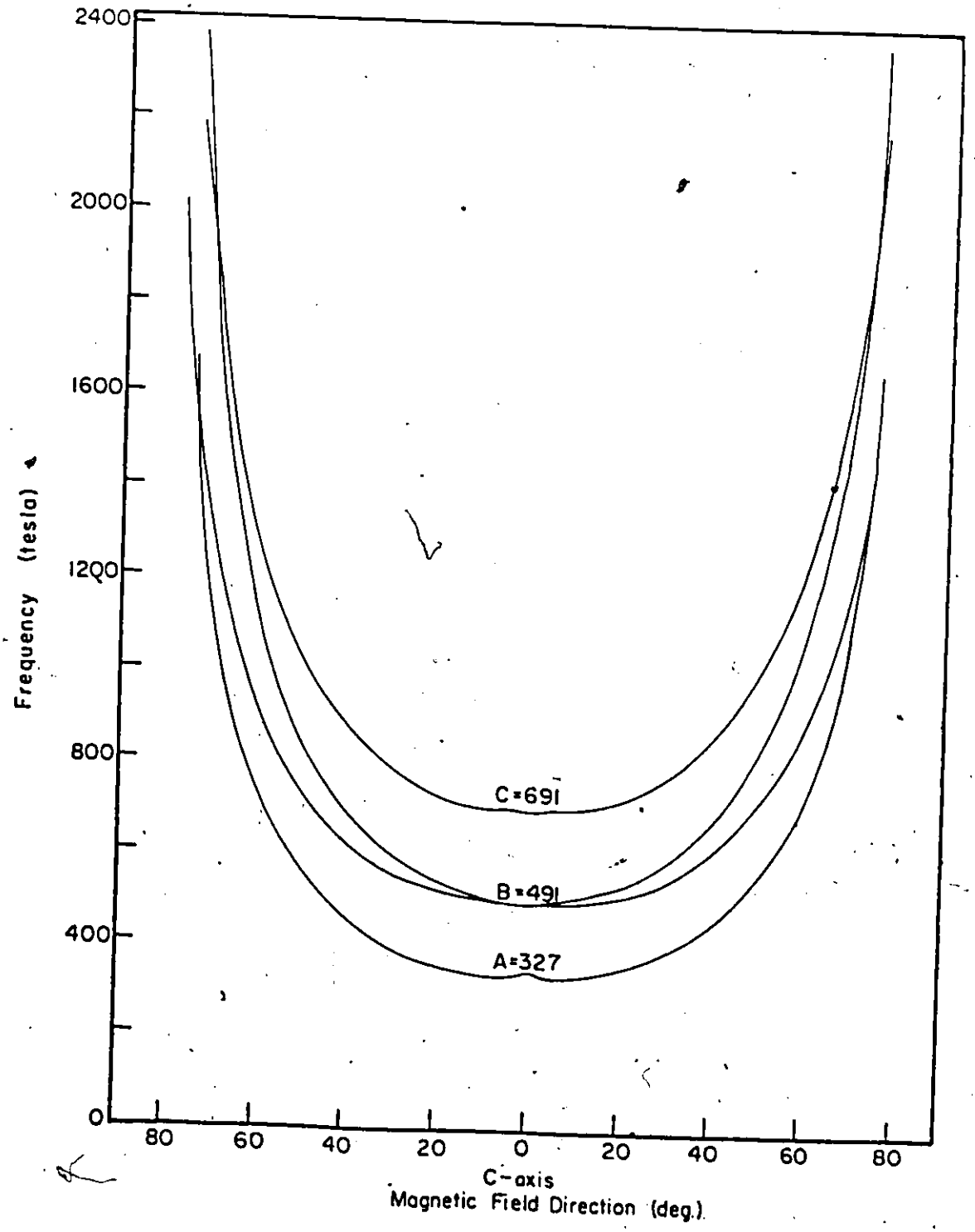
2400
2000
1600
1200
800
400
0
Frequency (tesla)
C=691
B=491
A=327
80
60
40
20
0
20
40
60
80
C-axis
Magnetic Field Direction (deg.)

Similar effects are expected to happen in $Hg_{3-\delta}AsF_6$. Table 8 shows an extremely good agreement between the calculated and the experimental results for γ and ε frequencies. This suggests that the γ and ε cylinders are the original Fermi surface sheets in Hg_3-δAsF_6 and the other Fermi surface sheets that were observed in the dHvA experiments arise from energy gaps produced by superlattice vectors with γ and ε Fermi surfaces.

Super lattices exist along the a and b directions of the tetragonal cell, because of the two non-intersecting and perpendicular chains of mercury in $Hg_{3-\delta}AsF_6$. Thus, we expect that the reciprocal lattice points in the tetragonal unit cell to be translated along the resultant vector $\sqrt{2}\ \delta^*$ of these two superlattice vectors.

The projection of the Fermi surface sheets on the (001) plane, Fig. 30(a), was translated by one super lattice vector $\sqrt{2}\ \delta^*$ and is shown in Fig. 30(b). The translation shown in Fig. 30(b) generates two hole-like orbits α and δ as well as a small electron-like orbit about 39 T. Fig. 30(c) shows the translation of the Fermi surface sheets by the superlattice vector $\sqrt{2}\ \delta^*$ in all four directions. Under these translations the δ orbit disappears and four α and four β orbits are produced and magnetic breakdown between α and β creates the δ orbit. This agrees with the experimental results since the δ frequency

Figure 30

(a) Projection of γ and ε Fermi surface sheet in ab plane.

(b) The translated γ and ε Fermi surface sheet along one of the directions of the superlattice vector $\sqrt{2}\ \delta^*$. Two hole-like frequencies α and δ as well as a small electron-like orbit were obtained.

(c) Full translation of the γ and ε Fermi surface sheets in all 4 directions of the superlattice vectors α, β, δ and ε are hole-like orbits and dotted area one electron-like orbits.

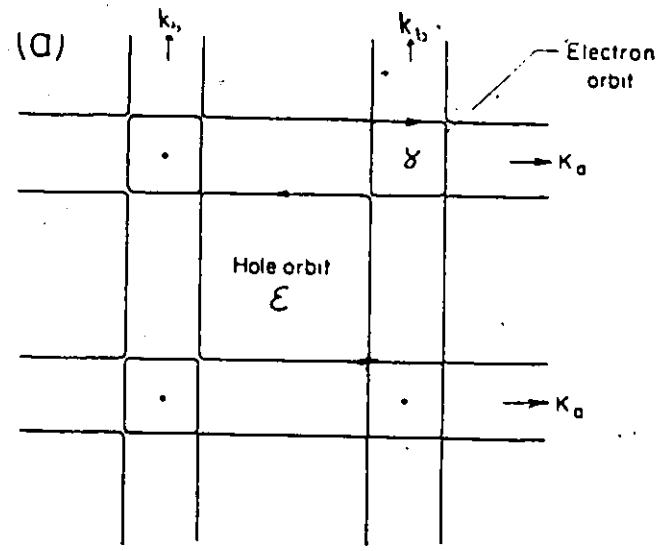
(a)
k_a
k_b
Electron orbit
γ
K_a
Hole orbit
ε
K_a

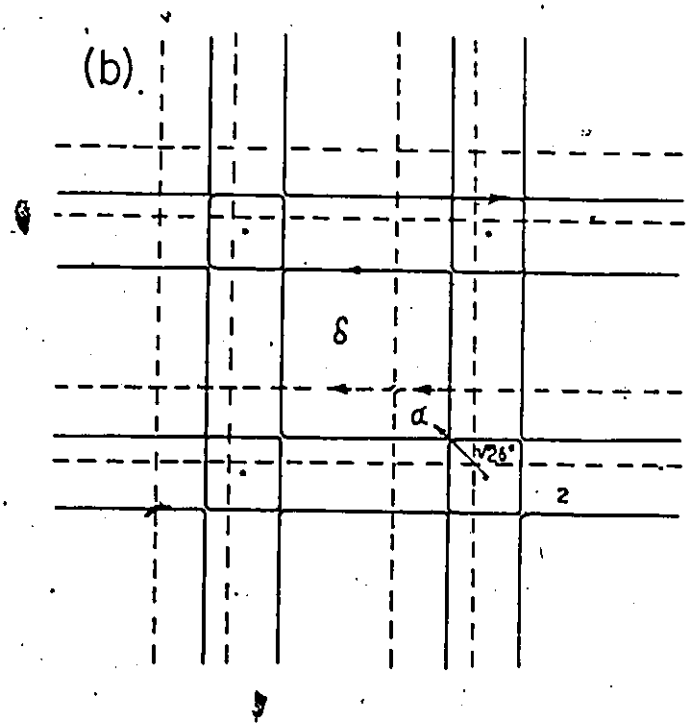
(b)
δ
α
2

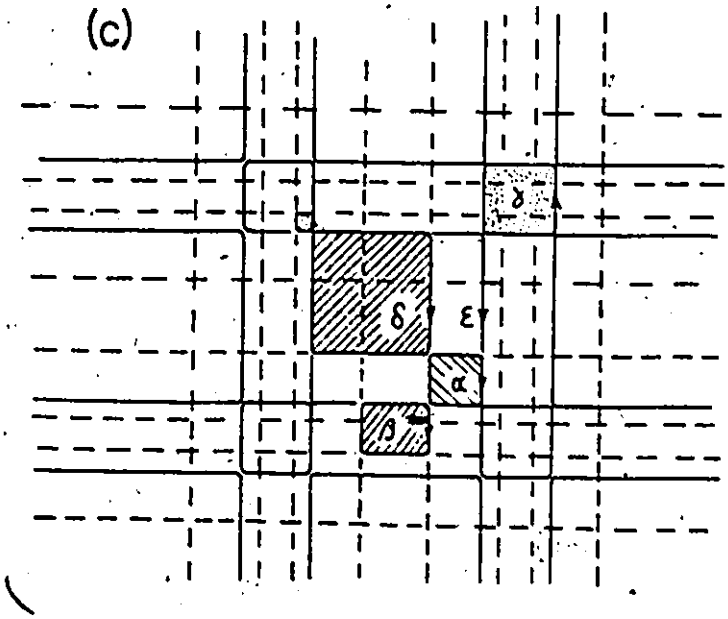
(c)
γ
δ
ε
α
β

was weak in all the magnetic field directions. All the frequencies which were generated by these translations are indicated in Fig. 30(c). It should be noted that because of the four fold symmetry of the lattice there are four orbits corresponding to each α, β and γ orbit which are not shown in Fig. 30(c).

The frequencies produced by this translation procedure are in good agreement with the experimental results. Both calculated and experimental results are compared in Table 9. The electron-like orbit with the value of 39 T also agrees with the frequency observed in the AM-FM effect. Branch μ is the only one not produced directly by our model. It arises from magnetic breakdown because it is only observed at high magnetic fields and over a small angular range about the $\vec{c}$-axis.

The similar cyclotron mass of δ and ε also confirms that the two frequencies belong to the same band. The low frequency observed in the dHvA spectrum and in the Dingle amplitude of the γ frequency, is also explained by a small frequency resulting from translation of the γ Fermi surface sheet. The increase in amplitudes of the dHvA frequencies and appearance of the harmonics and combinations of the frequencies in the slow cooling experiment are another evidence that the Fermi surface depends on the existence of a super lattice (Schlottmann and Falicov 1977).

Knowledge of the energy gap produced by the superlattice is required in order to estimate the field value in which the

Table 9. Comparison between calculated and experimental results of dHvA frequencies of $Hg_{3-\delta}AsF_6$

Frequency	Experimental		Calculated	
	A ($Å^{-2}$)	(tesla)	A ($Å^{-2}$)	(tesla)
α	0.0325	340	0.032	331
β	0.0395	413	0.043	455
γ	0.0598	626	0.060	627
δ	0.178	1860	0.178	1867
μ	0.326	3413	--	-
ε	0.352	3680	0.35	3762

breakdown occurs. However, the dHVa experiment at a higher magnetic field than 5.5 tesla may provide information about the breakdown field, in other words the energy gap.

BIBLIOGRAPHY

Alles, H., Higgins, R.J. and Lowndes, D.H. 1975. Phys. Rev. B, 12, 1304.

Alles, H. and Lowndes, D. H. 1973. Phys. Rev. B, 8, 5462.

Anderson, J. R., O'Sullivan, W. J., and Schirber, J.E. 1967. Phys. Rev. 153, 721.

Barrett, C. S. 1957. Acta Cryst. 10, 58.

Batalla, E. (1976). M.Sc. Thesis, McMaster University

Batalla, E. 1978. (private communication).

Berlinsky, R.J. 1978. Private Communication.

Brown, I.D., Cutforth, B.D., Davies, C.G., Gillespie, R.J., Ireland, P.R., and Vekris, J.E. 1974. Canadian J. Chem. 52, 791.

Chartier, D., Gillespie, J. 1978. (to be published).

Chiang, C. K., Spal, R., Denenstein, A., Heeger, A.J., Miro, N.D., and MacDiarmid, A.G. 1977. Solid State Commun. 22, 293.

Coleridge, P.T. and Templeton, I.M. 1972. J. Phys. F: Metal Phys. 2, 643.

Cutforth, B.D. 1975. Ph.D. thesis, McMaster University.

Cutforth, B.D., Datars, W.R., Gillespie, R.J., and van Schyndel, A. 1976. Adv. Chem. Ser. 150, 147.

Cutforth, B.D., Datars, W. R., van Schyndel, A., and Gillespie, R.J. 1977. Solid State Commun. 21, 377.

Datars, W. R., van Schyndel, A., Lass, L.S., Chartier, D. and Gillespie, R.J. 1978. Phys. Rev. Lett. 40, 1184.

Dupree, R. and Holland, B. W. 1967. Phys. Stat. Sol. 24, 275.

Dunsworth, A. E. 1972. Ph.D. Thesis, McMaster University.

Ehrenfreund, E., Newman, P.R., Heeger, A.J., Miro, N.D., and MacDiarmid, A.G. 1977. Phys. Rev. B16, 1791.

Falicov, L.M. and Zuckerman, M.J. 1967. Phys. Rev. 160, 372.

Fawcett, E. 1964. Advan. Phys. 13, 139.

Feinleib, J., Scouler, W.J., and Ferretti, A. 1968. Phys. Rev. 165, 765.

Ferretti, A., Rogers, D. B. and Goodenough, J. 1965. Phys. Chem. Solids, Pergamon Press, Vol. 26, pp. 2007-2011.

Goldstein, A., Williamson, S. J. W., and Foner, S. 1965. Rev. Sci. Instr. 36, 1356.

Goodenough, J. B., and Longo, J.M. 1970. In Landolt-Bornstein Tabellen, edited by Hellwege, K.M. and Hellwege, A.M. (Springer-Verlag, Berlin).

Graebner, J. E. and Marcus, J.A. 1968. Phys. Rev. 175, 659.

Graebner, J. F. and Greiner, E. S., 1969. Phys. Rev. 165, 765.

Graebner, J. E. 1977. Solid State Commun. Vol. 21, pp. 353-356.

Harrison, W. A. 1965. Proceedings of the First International Conference on the Physics of Solids at High Pressures (University of Arizona, Tucson, Arizona).

Harrison, W. A. 1966. Pseudopotentials in the Theory of Metals, Benjamin.

Hastings, J. M., Pouget, J. P., Shirane, G., Heeger, A.J., Miro, N.D., and MacDiarmid, A.G. 1977. Phys. Rev. Lett. 39, 1484.

Jennings, L. D., and Swenson, C.A. 1958. Phys. Rev. 112, 31.

Lifshitz, I.M., and Kosevich, A.M. 1955. Zh. Eksperim. Theor. Fiz. 29, 730 [Translation; Soviet Physics JETP 2, 636 (1956)]

Lifshitz, I.M., Azbel, M. Ya, and Kaganov, M.I., 1956. J. exp. theor. Phys. 30, 220 [translation: 1957, Soviet Physics - JETP, 3, 143].

Lifshitz, I. M. and Peschanskii, V. G. 1958. Zh. Eksperim. i Teor. Fiz. 35, 1251. [English transl: Soviet Phys. JETP 8, 875 (1959)].

Lifshitz, I. M. 1960. Zh. Eksp. Teor. Fiz. 38, 1569 [Sov. Phys. JETP 11, 1130 (1960)].

Logan, B. F., Rice, S. O., and Wick, R.F. 1971. J. Appl. Phys. 42, 2975.

Marcus, S.M. 1968. Phys. Letters 27A, 584.

M attheiss, L. F. 1969. Phys. Rev. 181, 987.

Mattheiss, L.F. 1972. Phys. Rev. B, 6, 4740.

Montgomery, M.C. 1971. J. Appl. Phys. 42, 2971.

Moss, J. and Datars, W.R. 1967. Phys. Letters 24A, 630.

Myron, M.W., Gupta, R.P., and Liu, S.K. 1973. Phys. Rev. B4, 1292.

Narath, A. and Barham, D.C. 1968. Phys. Rev. 176, 479.

Onsager, L. 1952. Phil. Mag. 43, 1006.

Pearsall, T. P., and Lee, C.A. 1974. Phys. Rev. B, 10, 2190.

Pearsall, T.P., and Coldren, L.A. 1976. Solid State Commun. Vol. 18, pp. 1093-1096.

Peebles, D. L., Chiangs, C.K., Cohen, M.J., Heeger, A.J., Miro, N.D. and MacDiarmid, A.G. 1977. Phys. Rev. B,15, 9607.

Phillips, R.A. and Shanks, H.R. 1971. Phys. Rev. B,4, 460.

Phillips, R.A. and Gold, A.V. 1969. Phys. Rev. 178, 932.

Pouget, J. P., Shirane, G., Hastings, J.M., Heeger, A.J., Miro, N.D., and MacDiarmid, A.G. 1978 (to be published, Phys. Rev. B).

Quinn, R. K., and Neiswander, P.G. 1970. Mat. Res. Bull. Vol. 5, pp. 329-334.

Randles, D.L., 1972. Proc. R. Soc. Lond. A, 331, 85.

Ražavi, F.S., and Datars, W.R. 1976. Can. J. Phys. 54, 845.

Schirber, J.E. and Switendick, A.C. 1970. Solid State Commun. 8, 1383.

Schirber, J.E., Morosin, B., Anderson, J.R., and Stone, D.R. 1972. Phys. Rev. B,5, 752.

Schirber, J.E., and Shanfeldt, D.W. 1968. Rev. Sci. Instrum. 39, 270.

Schlottmann, P., and Falicov, L.M. 1977. Phys. Rev. Lett. 38, 855.

Scholz, G. A., Datars, W.R., Chartier, D., and Gillespie, R.J. 1977. Phys. Rev. B, 16, 4209.

Shoenberg, D., 1962. Phil. Trans. Roy. Soc. (London) A255, 85.

Shoenberg, D. and Vuillemin, J. J., 1966. Proc. L.T. 10, Moscow, 3, 3107.

Shoenberg, D. 1969. Phys. Kondensierten Materie 9, 1.

Slavin, A.J. and Datars, W.R. 1974. Can. J. Phys. 62, 1622.

Spain, I.L., and Segall, S. 1971. Cryogenics, 11, 26.

Tsuda, N., Sumino, Y., Ohno, I., and Akahane, T. 1976. J. Phys. Soc. Japan, Vol. 41, 1153.

Verge, C., Altounian, Z., and Datars, W.R. 1977. J. Phys., E: Scientific Instruments, 10, 16.

Vischer, P.B., and Falicov, L.M. 1970. Phys. Rev. B,2, 1518.

Wei, T., Garito, A.F., Chiang, C.K., and Miro, N.D. 1977. Phys. Rev. B, 16, 3373.

Wilson, J.A. 1977. Phys. Rev. B 15, 5748.